NTNU
Norwegian University of
Science and Technology

Deposition of phase pure KNN thin Films

Kim Kristoffer Tolfsby Lorentzen

Materials Science and Engineering
Submission date: August 2016
Supervisor: Tor Grande, IMTE
Co-supervisor: Mads Jonas Christensen, IMTE

Norwegian University of Science and Technology
Department of Materials Science and Engineering

NTNU – Trondheim
Norwegian University of
Science and Technology

Deposition of phase pure $K_{0.5}Na_{0.5}NbO_3$ thin films

Kim K. Tolfsby Lorentzen

Spring 2016

TMT4905 - Materials Technology, Master's Thesis
Department of Materials Science and Engineering
Norwegian University of Science and Technology

Supervisor: Professor Tor Grande
Co-Supervisor: PhD candidate Mads J. Christensen

Acknowledgements

First and foremost, I want to sincerely thank my supervisor, Prof. Tor Grande, for his time and the opportunity to work under his guidance on this exciting project for my master's thesis, and for staying positive during long periods of negative results. The discussions we have had during our regular meetings have been invaluable to better my understanding of the topic. I would also like to thank Prof. Tor Grande for his cooperation and flexibility in the final stages of my thesis.

Secondly, PhD-candidate Mads J. Christensen, for his guidance in everything related to the experimental and analytical parts of my thesis, as well as being ever-present for a chat when needed. I am also thankful for his successful balancing of being both my co-supervisor and my friend. His ability to separate the two roles has been invaluable, both academically and socially.

I have thoroughly enjoyed this time working with both of my supervisors and I am genuinely sad to see it come to an end with the completion of my master's thesis.

A big thank you goes out to Mari-Ann Einarsrud who, alongside my supervisors, was vital during the initial stage of my thesis by helping me form a theoretical foundation and understanding of several possible origins of phase inhomogeneity in my samples.

Thank you to the staff of the K-II building and to those responsible for the clean room at NTNU for their introductory lecture and continuous support of the equipment in their respective labs. In particular Kristin Høydalsvik Wells, Magnus Rotan and Pei Na Kui from K-II; and from the clean room, Espen Rogstad, Eric Karhu, Mathilde Isabelle Barriet, Birgitte McDonagh and Ken Roger Ervik.

A special thank you goes to Kristin Høydalsvik Wells from K-II, and to Yingda Yu from the materials science building for their patience with me, as well as Yingda Yu's in-depth introductory lecture covering seemingly everything relating to SEM.

Also worthy of a mention here are the attendees of the weekly ferroelectric materials group meetings. I greatly appreciate their feedback and discussion during and after presenting my preliminary results - whether they were promising or not.

I would like to thank Dr. Achiri Tange, whose lectures on ferroelectric materials during my year abroad at University of Ulsan during spring 2014, sparked my initial interest in, an desire to further study ferroelectrics.

Acknowledgement goes to poLight AS for funding the Beat the Human Eye project, and to the Research Council of Norway for their support of the Norwegian Micro- and Nano-Fabrication Facility, NorFab.

And finally, a big thank you goes to Lynnée Lorentzen for once again finding the time and energy to proofread my paper.

Preface

The work reported in this paper was carried out in the period February 9 through August 8, 2016, and is a continuation of the work in the paper $K_{0.5}Na_{0.5}NbO_3$ deposition on platinized silicon substrates, written between August 25, 2015 and January 6, 2016, motivated by the persistent presence of the secondary phase $(K_{1-x}Na_x)_2Nb_4O_{11}$. Both papers are a part of the requirements for receiving a M. Sc. degree in materials science from the Department of Materials Science and Engineering at NTNU, Trondheim, and has been supervised by Prof. Tor Grande and PhD-candidate Mads J. Christensen.

All work was carried out by Kim K. Tolfsby Lorentzen, and the results obtained are part of the Beat the Human Eye project, funded by poLight AS.

Summary

Piezoelectric and ferroelectric materials have a wide range of applications, from touch and heat sensors to LCDs and actuators in MEMS. Lead zirconate titanate (PZT), is the most well-known ferroelectric material, and is the material of choice for such devices. Lead is a highly toxic heavy metal, affecting many life forms, including humans due to the body's inability to properly differentiate between Pb^{2+} and Ca^{2+}, and as a result, lead is able to enter the bones. Furthermore, lead poisoning can result in damage to the CNS, potentially leading to development of encephalopathy and severe mental impairments [1]. Due to its dangers, lead is banned within the EU for most applications today. However, as there currently is no suitable alternative to PZT, it is exempt from this ban [2]. Despite this exemption, there is an industry-wide desire to phase out the use of this compound in favour of more environmentally friendly alternatives.

In line with the desire for an industrially applicable and overall environmentally friendly alternative to PZT, this paper is focused on deposition of thin films from an aqueous potassium sodium niobate (KNN) solution by means of spin coating. The method synthesis route chosen is based on the works of K. N. Pham [3]. Obtaining phase pure films with this aqueous solution-based method has however been a consistent problem, and a challenging one to solve. Evidenced by XRD analysis, and observed through SE SEM, is the existence of a phase with tetragonal tungsten bronze structure and composition $(K_{1-x}Na_x)_2Nb_4O_{11}$. The phase is found on the film surface only. The origin of this phase has previously been poorly understood in the context of aqueous solution deposition of KNN thin films, however K. N. Pham found that there is an epitaxial Na-rich layer present in samples synthesized as per his paper [3]. Properly preventing the formation, or eliminating the effects of this epitaxial layer is thought to be crucial in eliminating the secondary phase, for when ignored its formation leaves the film stoichiometrically inhomogeneous.

This paper reports the results of three different approaches in an attempt to eliminate the existence or negative effects of this epitaxial layer. An increase in the pyrolysis temperature, from 400 °C to 500 °C and further to 550 °C was found to yield homogeneous nucleation of nano-sized KNN grains throughout the sample during pyrolysis. As a result, a significant reduction of the secondary phases was achieved, evidenced by XRD analysis. This approach has been found to yield dense films with an even surface and a thickness in the region 300-350nm, and is reproducible on both strontium titanate (STO) and platinized silicon substrates (SiPt).

The two other approaches reported in this paper, dealing with the stoichiometric alkali metal-deficit in the surface region, proved to be unsuccessful at reducing the presence of the secondary phase. An alkali rich solution was deposited and sintered on top of an otherwise finished sample pyrolyzed at 400 °C in an attempt to remedy the lack of alkali metals in the surface region by means of diffusion during re-sintering. Increasing the amount of alkali metals throughout the sample has previously been attempted on

STO, by K. N. Pham [3]. Due to the industry requiring the use of SiPt substrates, this approach was attempted on SiPt in order to help understand the different behaviours of the substrates in relation to KNN.

It has also previously been found through SEM analysis that there were some morphological issues, which have been attributed to the addition of polyvinyl alcohol (PVA) as a wetting agent, which is thought to affect the quality of deposited layers negatively [4]. This paper has instead successfully implemented the use of either an oxygen plasma cleaning or a piranha etching step before deposition of the solution to address the morphological issues caused by PVA, while maintaining good wetting with the substrate and a high quality of each coated layer.

Abbreviations

NTNU	Norwegian University of Science and Technology
STO	Strontium Titanate
SiPt	Platinized Silicon
SiPt-P	Platinized Silicon, cleaned with oxygen plasma
STO-P	Strontium Titanate, cleaned with oxygen plasma
SEM	Scanning Electron Microscope
FESEM	Field Emission Scanning Electron Microscope
XRD	X-ray diffraction
GIXRD	Grazing incidence x-ray diffraction
RTP	Rapid-thermal processing
T	Temperature, [°C]
T_C	Curie temperature, [°C]
A	The A-site cation in an ABO_3 crystal structure
B	The B-site cation in an ABO_3 crystal structure
MPB	Morphotropic phase boundary
PPB	Polymorphic phase boundary
PZT	Lead Zirconate Titanate, $Pb(Zr_xTi_{1-x})O_3$, $0 < x < 1$
NAmOx	Niobium Ammonium Oxalate
SiPt-x	Sample number, $x = 1, 2, ..., n$
STO-x	Sample number, $x = 1, 2, ..., n$
BSE	Back-Scattered Electrons
EDS	Electron Dispersive X-ray Spectroscopy
Sol-x	Solution-x, where $x = 1, 2, ..., n$
MEMS	Microelectromechanical systems
FCC	Face-centered cubic (unit cell)
EHS	Environment, health and safety
NN	Sodium niobate, $KNbO_3$
KN	Potassium niobate, $NaNbO_3$
BTO	Barium titanate, $BaTiO_3$
a, b, c	Axis directions and lengths in a unit cell
t	Goldschmidt tolerance factor
r_A	Radius of the A-site cation
r_B	Radius of the B-site cation
r_0	Radius of the anion, oxygen in a perovskite
P_s	Spontaneous polarization
LCD	Liquid Crystal Display
PVA	Poly-vinyl alcohol, $[CH_2CH(OH)]_n$
CNS	Central nervous system

Contents

1 Introduction

Background

Piezoelectricity dates back to 1880, when it was discovered by Jacques and Pierre Curie. Ferroelectricity, a sub-group among piezoelectrics, was discovered later, in 1921 in Rochelle salt [5]. Both, however have attracted significant scientific interest, especially post World War II, where piezoelectricity was applied in sonars [6]. More recently we have been able to merge science and industry by applying the functionality offered by ferroelectrics. Ferroelectric materials today have a wide range of applications primarily within MEMS; ranging from touch and heat sensors to FeRAM, LCDs, gas ignitors and speakers [5, 7–10]. PZT, the most well-known ferroelectric material, is generally the material of choice for such devices due to its superior piezo- and ferroelectric abilities.

poLight AS is a Norwegian company located in Horten. Since 2006 poLight AS has been developing technology related to cameras for smart phone use. The current iteration of their smartphone camera lens is called TLens, currently equipped with a PZT-based actuator responsible for controlling the curvature of the lens, and thus the focal point. The application of the piezoelectric actuator is illustrated in figure 1 [11]. The standout features of cameras based on piezoelectric actuators are very rapid change of focus, in the order of 1 ms, and significantly reduced power consumption when compared to conventional smart phone camera technology [11, 12]. The TLens relies solely on the piezoelectric property of its actuator, but ferroelectric materials are still favoured for piezo-applications due to their superior electromagnetic coupling, which makes PZT the preferred choice.

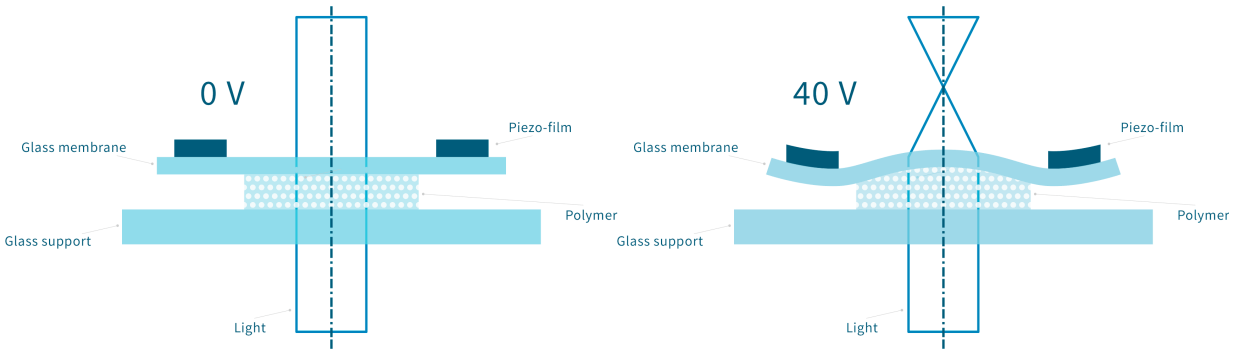

Figure 1: Illustration of the TLens, and how the inverse piezoelectric effect of the actuator is applied to obtain focus.

PZT does however contain lead – a highly toxic heavy metal affecting many life forms, and thus the continued use of PZT is cause for serious health and environmental concern. The most dangerous symptoms of lead poisoning in humans are damage to the CNS, potentially leading to development of encephalopathy and severe mental impairments. [1]

As a result, lead is banned from industrial use for most applications in the EU. Due to the lack of suitable alternatives however, PZT is currently exempt from this ban. There is still a general industry-wide desire to phase out the use of lead-containing compound in favour of more environmentally friendly alternatives – in part due to the desire for a greener profile, but also in preparation of the eventual reimplementation of the ban on PZT. Regardless of the environmental hazard that comes along with lead-based compounds, PZT remains a mainstay in technology due to its superior performance.

The Beat the Human Eye project started in 2014 with the goal of improving the performance of the TLens as a whole by increasing the opacity of the lens, but also to replace the lead-containing actuator with a high performance lead-free alternative. There are currently several lead-free compounds being investigated in hopes of matching the performance of PZT – one of these is barium titanate (BTO).

BTO was the first polycrystalline ceramic perovskite in which ferroelectricity was observed, in 1944. The origins of ferroelectricity may differ between different compounds, and such is the case for PZT and BTO. [5] Generally, in compounds where ferroelectric behaviour can be observed, it is found to increase when compositions lie near a phase boundary. While under static conditions there may seemingly be insignificant differences between the two, this is not the case for real-world applications where temperature in particular, but also mechanical properties as well as chemical stability and reactivity with the surroundings may affect the final choice. This is where PZT tends to have the upper hand over most other ferroelectrics. While the ferroelectric behaviour of BTO is found in the vicinity of a polymorphic phase boundary (PPB), PZT ferroelectrics lie near a morphotropic phase boundary (MPB). As such, the temperature stability of PZT is far superior to BTO. With the combination of BTO's Curie temperature reported between 115 °C [13] and 125 °C [14, 15] and having a significantly lower electromechanical coupling factor [5], PZT is generally the preferred choice since temperature instability and performance is often a bigger issue than chemical instability. BTO can be doped or otherwise modified by other compounds to help alleviate some of its problems, primarily relating to the lack of temperature stability, however it remains a fact that the piezoelectric performance is subpar in comparison to PZT [16, 17]. These factors, in addition to simpler manufacturing [5], led to PZT gaining increasingly more traction as a research subject over BTO, and is evidenced by the superior performance seen today.

In 2004, yet another candidate came up as a lead-free, environmentally friendly replacement for PZT – potassium sodium niobate (KNN), a compound of potassium (KN) niobate and sodium niobate (NN). This compound has been on the receiving end of scientific research for a long time [18], but without the performance to rival that of PZT. It wasn't until Saito *et. al.* [19] theorized the possible existence of a tetragonal-orthorhombic MBP in KNN similar in nature to that found in PZT, for compositions near 1:1 KN:NN, and achieved a significant performance breakthrough in the piezomechanical coupling with $d_{33} = 416\ pC/N$. At the time, the performance rivalled that of typical actuator-grade PZT, but recently PZT has seen an increase in performance, with reported d_{33} values of 660 pC/N [20].

Motivated by the promising results achieved by the *et. al.*, KNN has been receiving significant attention, and also seen performance increases in d_{33}, but to a lower degree than PZT, with reported values of 490 pC/N [21]. It is then understandable that the PZT-exemption from the EU lead-ban is upheld, and that poLight AS finds it necessary to use PZT in their TLens to remain competitive. Even so, KNN remains a strong candidate as an environmentally friendly PZT replacement, and optimizing its performance may enable poLight AS to replace their PZT actuator with one based on KNN.

KNN thin films are commonly deposited using liquid deposition methods, however they are often based on organic solvents rather than water. As a member of the Beat the Human Eye project, NTNU has taken an environmentally friendly approach to finding a solution, and as such has chosen to focus on developing an aqueous solution-based approach for KNN thin film deposition, initially detailed in a paper by K. N. Pham [3].

Aim of the work

With both practical as well as economical concerns in mind, it is a necessity for poLight AS that the new synthesis method of their thin film actuator is based on deposition of the thin film onto a SiPt substrate – the industrial standard. K. N. Pham's paper takes a sol-gel approach and focuses on KNN deposition by means of spin coating onto STO substrates. This paper aims to take the approach developed by K. N. Pham, and make necessary modifications as to optimize performance of the KNN thin film deposited onto SiPt substrates, making them applicable for use with the TLens.

STO is the preferred substrate for deposition of perovskite-type ferroelectric thin films, as it too has a perovskite structure, thus lessening the potential problems arising from substrate-film interactions. The SiPt substrate has a Si with a diamond cubic structure, but presents an FCC structured platinum surface for films to be deposited onto, in an attempt to lessen the effects of both lattice and crystal structure mismatches with KNN. The lattice differences, and thus the potential for problems associated by substrate-film interactions between platinum and KNN however, is still more significant than that of the STO-KNN system.

Furthermore, in the paper by K. N. Pham [3], there were persistent problems relating to phase purity in the thin films synthesized. More specifically, the formation of the tetragonal tungsten bronze (TTB) phase $(K_{1-x}Na_x)_2Nb_4O_{11}$ – a phase that was found to exist only on the film surface. Elimination of this phase is vital to the successful implementation of a KNN-based actuator in the TLens. Many routes were taken in an attempt to eliminate or prevent this phase from forming, with no significant and reproducible results returned [3]. This paper will focus primarily on attempting to solve this problem by further exploring the area, using both STO and SiPt substrates.

Finally, the samples will be analyzed with respect to phase purity by means of x-ray diffraction, with both Bragg-Brentano and grazing incidence configurations. SEM, with SE and EDS detectors will be used to analyse the homogeneity and morphology of the samples.

2 Theory

2.1 Crystal structures

There are many different ways for atoms to combine to form a material. Materials which consist of an ordered system of atomic positions are considered to be crystalline. The crystalline materials can be classified according to which symmetries the crystal exhibits, and there is a total of 230 distinct such groups, called space groups. For the purpose of simplification, these can be reduced to 32 through symmetry considerations, where 21 of these are non-centrosymmetric, and 20 exhibit piezoelectric properties. Of these 20 space point symmetry groups, 10 will also be polar, and pyroelectric – allowing a change in polarization when experiencing changes in temperature.

Ferroelectrics are yet again a sub-group of pyroelectrics, exhibiting all the previously mentioned characteristics of both pyro- and piezoelectric materials, but capable of maintaining the polarization even upon removal of the external field. Given the structurally meta-stable origin of polarization in perovskite ferroelectrics, the direction of the polarization can also be reversed [22]. A graphic illustration of the relation between the different classes of materials is shown in figure 2.

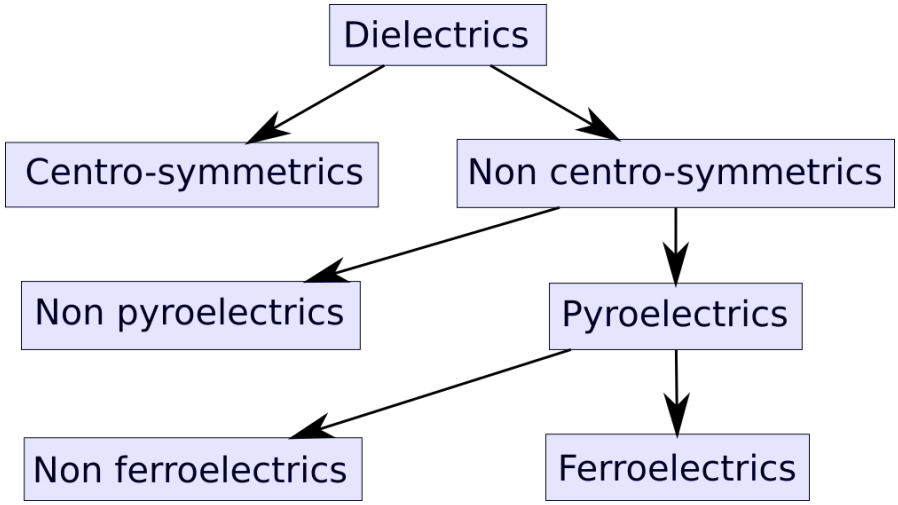

Figure 2: Graphic representation of the relations between the di-, piezo-, pyro- and ferroelectric classes of materials.

Ferroelectric ceramics can be found with four different crystal structures, namely perovskite, pyrochlore, tungsten bronze and bismuth-layer structures [23]. Out of these structures, most ferroelectrics are found within the perovskite group [5], containing compounds such as KNN, PZT and BTO among others. With respect to the scope of this paper, atomic models of the perovskite and tungsten bronze structures are illustrated in figure 3a and 3b respectively.

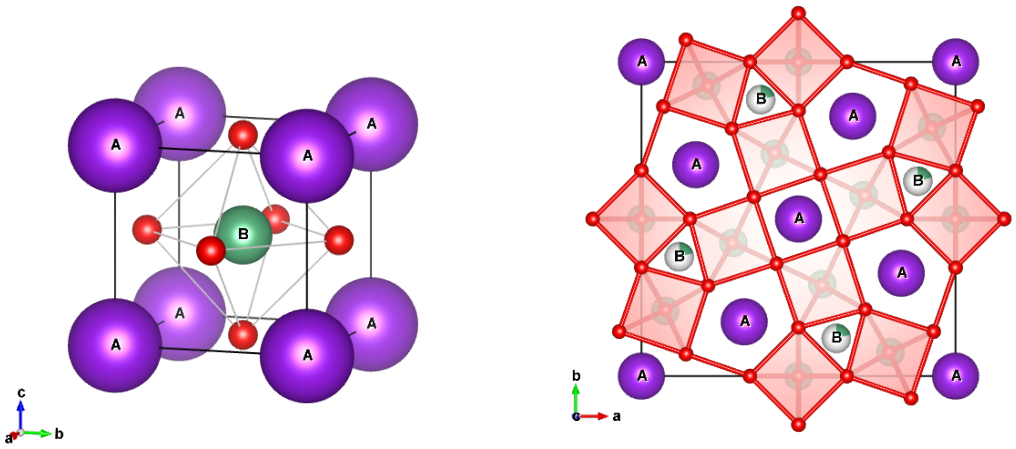

(a) Perovskite structure.

(b) Tetragonal tungsten bronze structure, with partially filled B-sites.

Figure 3: Illustrations the (a) perovskite and (b) TTB crystal structures.

Perovskites are a family of materials with the structure of the mineral $CaTiO_3$, which bears the same name. Perovskite was discovered in 1839 by geologist Gustav Rose, but is named after the Russian mineralogist, L. A. Perovski. As a crystalline structure, it is any compound with an ABX_3 composition of elements, where both A and B are metallic cations and X is a non-metallic anion [24]. In the case of ceramic ferroelectrics, the X element is often oxygen, in which case the formula is often written as ABO_3.

2.2 Piezoelectricity

A piezoelectric material is one which experiences the piezoelectric and converse piezoelectric effect. When a material is subject to an external force and it responds by producing a charge, it is said to be piezoelectric. Conversely, it follows that the material will also experience a physical change of dimensions when affected by an external field. The piezoelectric effect for a purely piezoelectric material is a temperature independent property of a solid, and strictly dependant on the crystal structure. An example of a structure which would exhibit piezoelectricity for all solid states can be seen in figure 4. Given its structure, it is understood that upon application of strain and subsequent deformation of the structure, there follows a change in net polarization which disappears upon relaxation. Conversely, during the application of an external field, the material will acquire a net polarization through deformation, which disappears when the field is removed.

The relationship between polarization of a piezoelectric and the applied stress can be expressed as $P = d_{ijk}\sigma_{jk}$ where d_{ijk} is the 3rd rank piezoelectric tensor, and σ_{jk} is the

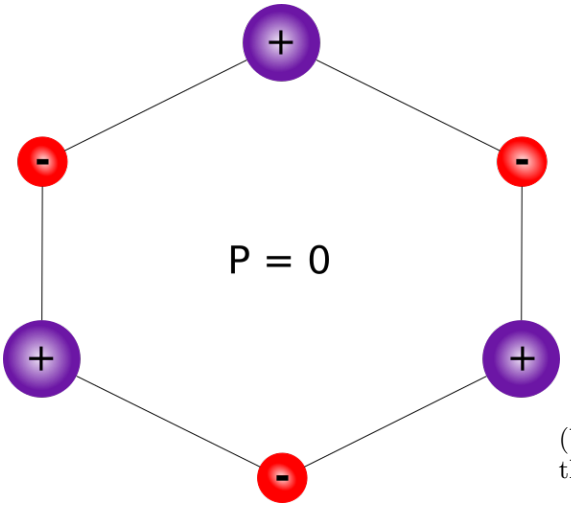

(a) Piezoelectric structure.

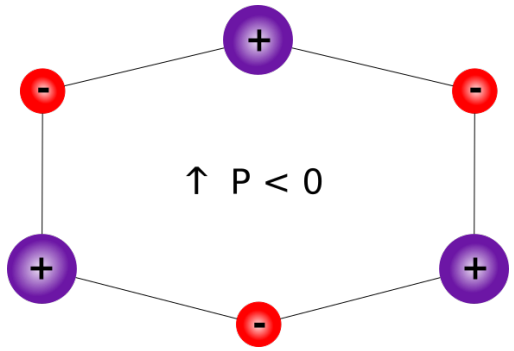

(b) Piezoelectric structure under pressure along the vertical axis.

Figure 4: Illustration of a piezoelectric structure illustrating how the structure and polarization is changed when the structure is deformed under pressure.

2nd rank stress tensor. Through thermodynamic arguments coupled with the Neumann principle, stating that no tensor describing a physical symmetry of a crystal can exhibit any less symmetry than that of the crystal itself, a reduction of tensors can be achieved. In the case of e.g. tetragonal symmetry, four tensors are sufficient – d_{15}, d_{22}, d_{31} and d_{33}, whereas for cubic symmetry, only two are required for the longitudinal and transverse response, respectively d_{33} and d_{31} [25].

2.3 Ferroelectricity

To better understand how piezoelectric and ferroelectric materials differ, it is important to keep in mind that the origin of piezoelectricity differs. The temperature below which ferroelectric materials exhibit ferroelectric properties is termed the Curie-temperature, T_C. For ferroelectric perovskite above the Curie temperature the unit cell is cubic, allowing no spontaneous polarization and is in essence a symmetric, paraelectric material. Below the Curie temperature however, there is a distortion of the axis length relations, often towards an orthorhombic or tetragonal structure which is ferroelectric, thus also exhibiting piezoelectric properties.

Consider the ABO_3 perovskite cell. As the central B-site atom is no longer equally affected by the presence of the surrounding oxygen atoms, after entering a phase located below the Curie temperature, a spontaneous shift in the equilibrium position of the B-site occurs perpendicular to the plane formed by the 4 most closely positioned oxygen atoms in the oxygen octahedra, figure 5. It is understood that there is a strong correlation between the displacive polarization, and the degree of displacement of the B-site atom,

where a larger displacement yields a higher polarization.

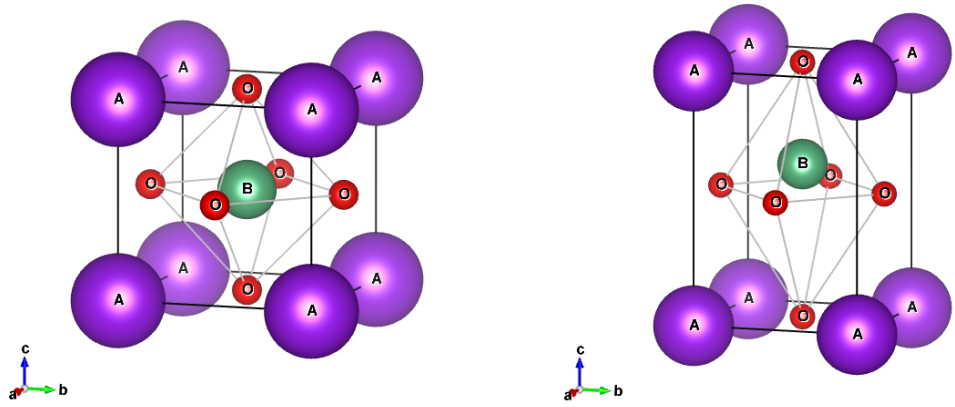

(a) The perovskite structure above the Curie-temperature.

(b) The perovskite structure below the Curie-temperature.

Figure 5: Illustration of how the central B-site atom is the origin of displacive ferroelectricity when the structure enters a (b) ferroelectric phase from the (a) paraelectric phase, here illustrated by a shift in the positive c-direction.

For the displacement of the B-site atom to occur, it is necessary that the structure is tightly packed and non-cubic, so that there are sufficiently strong repulsive forces between the atoms to the point where an off-centered position of the B-site atom is energetically favourable. The new, meta-stable positions are energetically equal, separated by an energy barrier with a peak in the centre of the unit cell. As the energy barrier is affected by the density of the unit cell, the stability of the displacements is positively correlated with ΔT, where $\Delta T = T_C - T$ [13]. It is understood that when the B-site atom is displaced in a ferroelectric, the structure is also piezoelectric, as illustrated by figure 6.

Below the Curie-temperature, ferroelectrics are always microscopically polar. Macroscopically however, this is initially never the case, as the individual orientation of the grains as well as the positive or negative displacement are oriented as to cancel the surrounding contributions, thus lowering overall surface energy [26]. The result is a net zero polarization in a bulk sample, illustrated in figure 7a by the randomly oriented directions of polarization. To ensure alignment of the individual grains' contribution to polarization, it is necessary to pole the material.

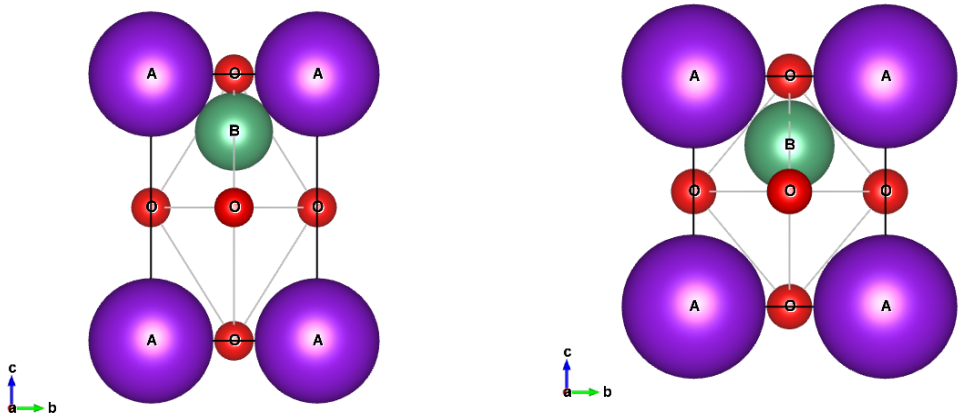

(a) Relaxed ferroelectric perovskite.

(b) Ferroelectric perovskite under applied pressure along c-axis.

Figure 6: Illustration showcasing the piezoelectric property in a ferroelectric perovskite – the (a) distance between the B-site atom and the unit cell center in its equilibrium state is (b) decreased when under pressure, thus the polarization is also affected by the pressure.

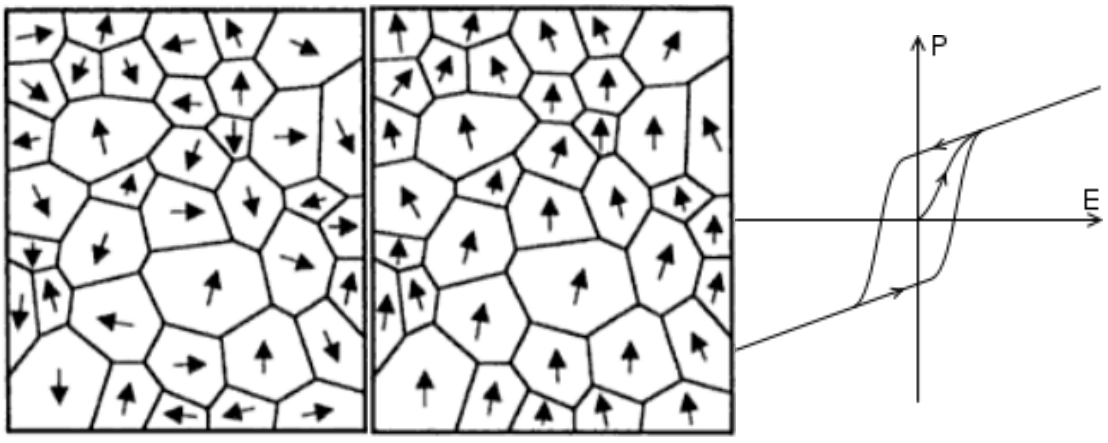

(a) Before poling.

(b) After poling.

(c) Hysteresis loop.

Figure 7: Illustration of the orientation of polarization in the grains of a ferroelectric material (a) prior to poling, and (b) after successful poling. The hysteresis loop of a ferroelectric being poled, then having its polarization switched by reversal of the applied field is shown in (c).

Poling is done by applying an electric field of significant strength, thereby forcing the B-site atoms into the currently most energetically favourable positions. The orientation of polarization can be switched, as discussed previously, however the process of poling is permanent, as the positions of the B-site atoms during poling are separated from the other equally favourable positions by the energy barrier. The polarization from the individual grains are at their maximum, both before and after poling. The overall polarization however increases after poling, but will always remain below its potential maximum, as the orientation of the grains can not align as easily. Figure 7b illustrates the resulting partial alignment of grains, yielding a net polarization after successful poling. During poling, the B-site atoms may be pulled further away from the centre than where their equilibrium position is, yielding a temporarily higher overall polarization, but this effect disappears along with the field, when the material returns to a state of rest, exhibiting remnant polarization, as per figure 7c.

2.4 Antiferroelectricity

Antiferroelectrics are somewhat different from normal ferroelectric materials. In understanding the phenomena that are antiferroelectric structures, it is necessary to study the structure on an atomic scale. When doing so, it becomes apparent that the structure is in fact built up of layers of atoms with oppositely aligned polarization. As such, it is often considered as built up by two separate, but intertwined sub-lattices. To form a unit cell, several sub-lattices are combined, adjacent to each other, as per figure 8a.

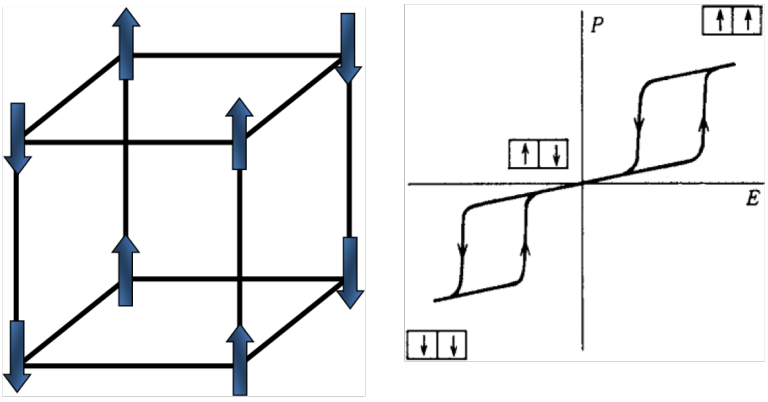

(a) An antiferroelectric unit cell.

(b) Antiferroelectric hysteresis loop.

Figure 8: Illustration of the oppositely aligned rows of polarized cations in an antiferroelectric unit cell, and (b) the hysteresis loop of an antiferroelectric.

Due to the antiparallel alignment of polarization of the intertwined unit cells, the antiferroelectric will not posses a macroscopic polarization. Since the net polarization is zero, the structure is not piezoelectric, but the structures do indeed become spontaneously polarized below the Curie-temperature [27, 28]. Antiferroelectrics can, however exhibit ferroelectric properties when under the effect of a strong applied field, forcing the oppositely charged polarizations to re-align temporarily. As such, a hysteresis loop similar to that found in ferroelectrics does occur in antiferroelectrics, figure 8b.

2.5 Goldschmidt tolerance factor

The Goldschmidt tolerance factor, $t = \frac{r_A + r_0}{\sqrt{2}(r_B + r_0)}$ [29], states whether the ionic radius of the B-site atom is cause for distortion of the perovskite unit cell. A perfect, relaxed perovskite has $t = 1$, whereas t values above or below 1 yields distortion of the unit cell, which can lead to new properties [30]. It is understood from the formula that higher t-values are caused by a smaller-than-ideal B-site atom radius, whereas smaller values stem from larger-than-ideal B-site atoms. The t-value is then inversely correlated to unit cell density.

Motivated by the misfit strain originating around the smaller B-site atom, the unit cell tends to experience distortion. Caused primarily by Coulumb interactions between the atoms, the perovskite unit cell tends to distort in favour of tetragonal-like structures. In part due to the increased $\frac{c}{a}$ unit cell ratios, but also the smaller B-site atom, the average density also sees a decrease with increasing t-values, which tends to increase displacive polarization. However, materials exhibiting ferroelectricity which also have a low t-value, benefit from the stronger atomic bonding due to the increased packing factor that occurs. The stronger bonding occuring for low t-value ferroelectrics generally results in higher stability of the structure, thus also a higher Curie-temperature [30, 31]. For t-values above 1.065 however, the unit cell tends to abandon the perovskite structure altogether, in favour of a different configuration that allows a lower energy. It is generally found that perovskites with $t \geq 1$ which exhibit ferroelectric properties are of composed of either the I-V or II-IV element groups [32]. $KNbO_3$, $PbTiO_3$ and $BaTiO_3$ are notable perovskites where the displacive ferroelectricity phenomena can be observed [30, 33], and an illustration of such a structure is shown in figure 5b.

Antiferroelectricity however, is more common when $t < 1$ – although there are exceptions to both scenarios, one of which is the ferroelectric $BiFeO_3$ with $t = 0.55$ [30, 31]. $t < 1$ occurs when the B-site atom is too large to properly fit the structure. While for higher t-values the B-site atom is free to displace within the oxygen octahedra, for low values the octahedra itself will distort originating in the strong atomic bonding caused by the very low interatomic distances, illustrated in figure 9. As is the case with ferroelectrics, antiferroelectrics will too tend to experience an inverse relationship between the t-values, and their T_C [34]. Due to the size of the B-site atom in $t < 1$ structures, and since size is generally highly correlated with the number of electrons, it is also a significant

contributor to the overall electronic polarization of the material. As such, P_s may be seen to incerase for low values of t – not only in antiferroelectrics, but also in regular ferroelectric materials. [30] Antiferroelectricity is most often found in II-IV and III-III perovskites with $0.86 \geq t < 1$, below which the perovskite tends to break down in favour of other, more stable structures such that of the hexagonal $YMnO_3$ system [32]. $NaNbO_3$ [28, 30, 35] and $PbZrO_3$ [28, 30] are examples compounds with a low tolerance factor, capable of anti-ferroelectricity.

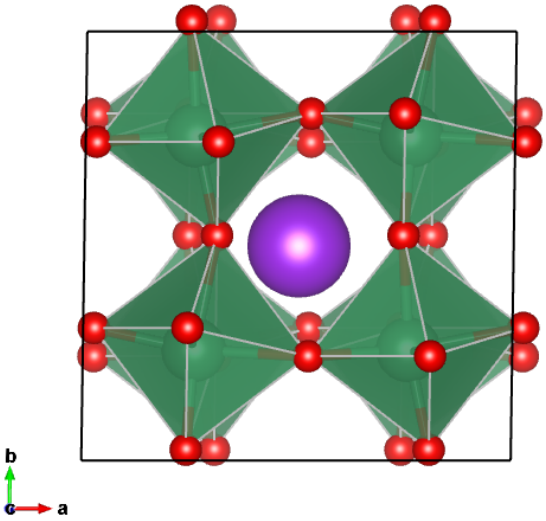

Figure 9: Illustration showing how the oxygen octahedras are distorted in a structure with large B-site atoms.

2.6 Phase boundaries

The degree to which a unit cell contributes to the overall polarization of a ferroelectric depends highly on the angle between the axis along which the B-site atom displaces and the macroscopic direction of polarization. When they are perfectly aligned, the contribution from the unit cell in question is additive to the overall polarization. The better the atom is able to accommodate the forced direction of of polarization during poling, the higher the net polarization. During phase changes, the material is in limbo between two or more different structures or compositions, allowing for more directions of polarization. As such, net polarization in ferroelectrics relying on displaced atoms is generally stronger in the vicinity of phase boundaries, regardless of the type of phase boundary.

Polymorphic phase boundaries

Polymorphic phase boundaries are temperature dependant phase boundaries. Utilizing them as a means of increasing the ferroelectricity in a material is often a challenge. Not because they offer small performance increases, but rather the intrinsic temperature instability that follows when taking advantage of them. Thus the practical applications of PPB's are quite limited in all devices that require operation at varying temperatures, or experience significant heat output during use. Furthermore, PPB's are often found not at room temperature, but below and above, and require doping to successfully harvest the benefits of the PPB at room temperature, making the synthesis potentially more difficult [13]. Materials utilizing PPB's to increase their performance are especially poor choices for memory devices due to the imminent risk of data corruption in addition to future malfunction, should the temperature variations become too large.

In situations where temperature variations are not a significant issue, there are several potential material systems. $BaTiO_3$ is one ferroelectric that relies on the presence of a PPB and a relatively low Curie temperature phase boundary, reported between $T_C = 115\,°C$ [13] and $T_C = 125\,°C$ [14, 15]. The low temperature of the PPB makes it a good candidate for doping, which could bring the PPB down to near room temperature [13].

Morphotropic phase boundaries

Morphotropic phase boundaries are composition-limited. Reactions with the environment or evaporation is for most applications a non-issue. As such, ferroelectrics taking advantage of MPB's generally offer significantly better stability than ones utilizing the presence of a PPB, regardless of whether the application is piezo- or ferroelectric in nature. For piezoelectric applications in particular, MPB's are preferable, as compounds relying on them often exhibit superior electromechanical coupling [35]. As for pyroelectric applications, they are often the only choice, due to the range of temperatures that may be necessary during operation.

Most phase boundaries are however not pure PPB's or MPB's, but rather a combination of the two. The degree to which they are one or the other can vary significantly, effectively limiting their use. Successfully stabilizing either the temperature or composition instability is often critical to successful implementation. $PbZr_xTi_{1-x}O_3$, whose phase diagram is available in figure 10 [35], is one material system utilizing a phase boundary that is naturally almost entirely polymorphic in nature, which is cause for its popularity and allows its use within such a wide range of applications [35].

2.7 $K_{0.5}Na_{0.5}NbO_3$

After the discovery of polycrystalline ceramic ferroelectrics, starting with $BaTiO_3$ in 1944, several others would soon follow – among them, $K_{0.5}Na_{0.5}NbO_3$ in the 1950s [15, 35]. It would however take almost 50 years before it gained significant attention, as a potential $Pb(Zr_xTi_{1-x})O_3$ replacement.

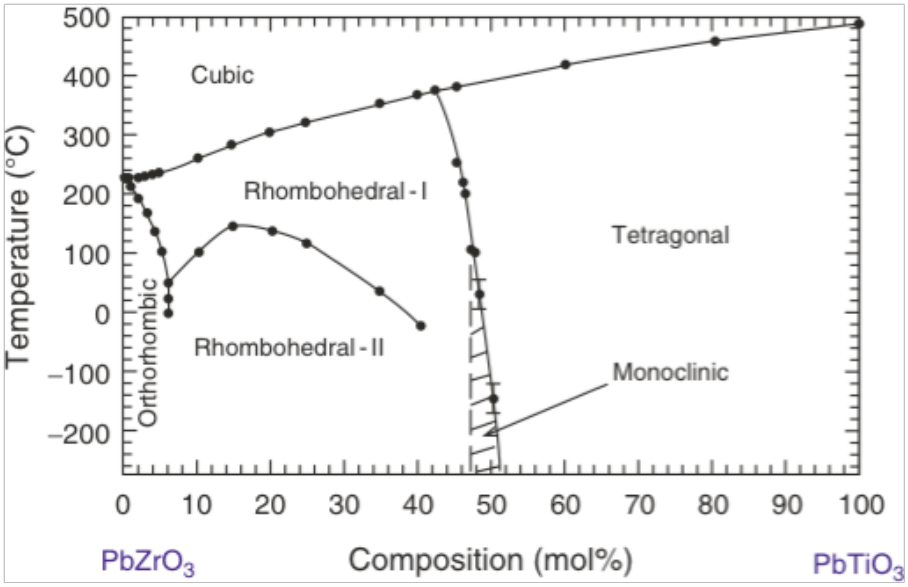

Figure 10: Phase diagram between $PbZrO_3$ and $PbTiO_3$.

In 2004, Saito *et. al.* [19] managed a performance breakthrough in $K_{0.5}Na_{0.5}NbO_3$, by significantly increasing the electromechanical coupling factor to $d_{33} = 416\ pC/N$, thereby more than doubling that of undoped $Pb(Zr_xTi_{1-x})O_3$ at the time of Saito's breakthrough, $d_{33} = 200\ pC/N$. To achieve this breakthrough, successful utilization of several techniques were necessary. In particular textured growth, thereby allowing near perfect alignment of the individual grains and thus also the spontaneous polarization after poling. Untextured compounds of the same KNN-based material systems generally exhibit lower electromechanical coupling factor, with d_{33} near 300 pC/N [19, 35] Additionally, the presence of an MBP between the pseudo-ilmenite and perovskite structures was utilized in the perovskite-rich region [19]. Later research suggests however that the optimal ratio of sodium and potassium in doped KNN is not at 0.5:0.5, but rather 0.48:0.52 K:Na, and that this composition takes advantage of the MPB between the monoclinic and orthorhombic phases [21, 35–38]. With further modification of the KNN system, using $LiTaO_3$ and $LiSbO_3$, the PPB at the tetragonal - orthorhombic interface is moved down towards room temperature from about 200 °C for the pure $K_{0.5}Na_{0.5}NbO_3$, as seen in figure 11 [35], allowing further improvements to the properties of the KNN-based compound. The combination of a PPB with a MPB allows a relatively high degree of orientational freedom in comparison to that of the undoped system, and one can see the results of the careful engineering in the improvements to the d_{33} value, from about 300 pC/N to 416 pC/N. With this in mind, it then becomes obvious that making further improvements to KNN-based compounds is a challenge, and careful engineering of all variables involved is necessary in order to maximize the total combined contribution.

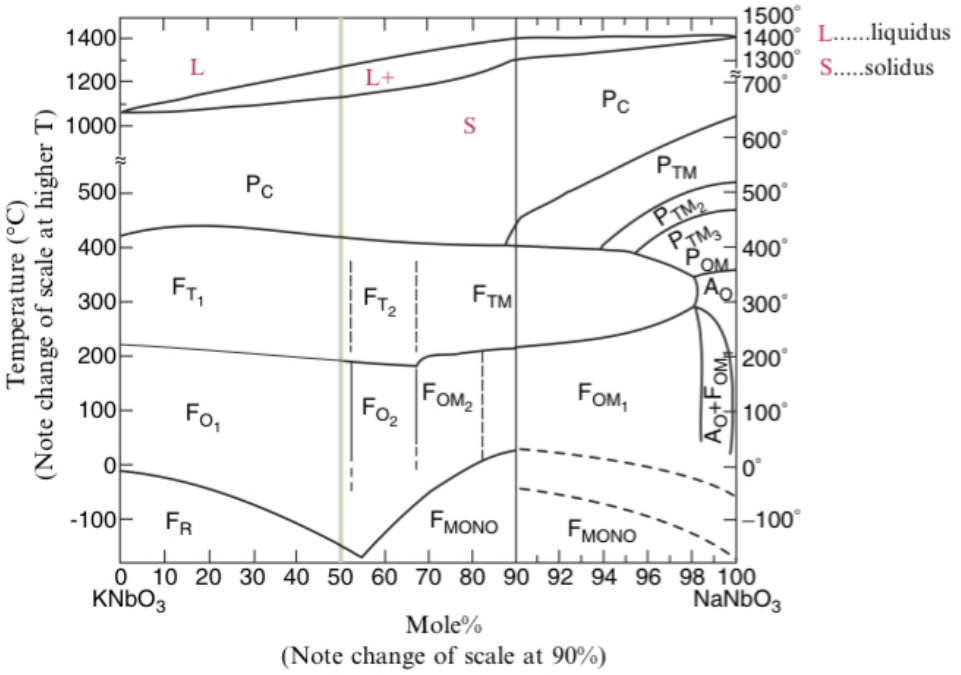

Figure 11: Phase diagram between $KNbO_3$ and $NaNbO_3$.

Since 2004 however, no single equally significant performance breakthroughs have been made, despite increased interest in both KNN and lead-free ferroelectrics in general. In 2014, KNN compounds had reached a $d_{33} = 490\ pC/N$, achieved by X. Wang *et. al.* [21] with the compound $0.94(K_{0.48}Na_{0.52})(Nb_{0.95}Sb_{0.05})O_3 - 0.06Bi_{0.5}(Na_{0.82}K_{0.18})_{0.5}ZrO_3$. The success stems in part from the successful phase boundary engineering, moving the tetragonal – orthorhombic transition temperature downwards, and simultaneously moving the orthorhombic – rhombohedral transition temperature upwards, by additions of $(Bi_{0.5}(Na_{1-x}K_w)_{0.5})^{2+}$ and Zr^{4+} respectively. The compound has a Curie-temperature of $T_C = 227\,°C$, which is a significant decrease from that of the pure orthorhombic KNN, $T_C = 450\,°C$ [19], but near that of the doped and textured breakthrough compound by Saito *et. al.*, with $T_C = 253\,°C$ [19].

The main problems regarding KNN synthesis are related to stoichiometry, in that alkali metals are notoriously difficult to contain in compounds experiencing high temperatures, and tend to evaporate [35, 39, 40]. Potassium and sodium have boiling points at 758.8 °C and 882.9 °C respectively [41]. While the boiling point of sodium is higher than that used for heat treatment in this work, it too has a high vapour pressure, hence it too will experience evaporation, and has been reported doing so at a higher rate than potassium at very high temperatures [42]. As such, it is difficult to maintain control over the exact ratios in the final compound, as they often differ from that of the solutions used. In particular thin films are affected by this problem, as the surface to

volume ratio is significantly higher than in bulk materials, allowing a much higher rate of evaporation. As a result of the often stoichiometrically A-site deficient KNN post heat treatment, compared to that found in the KNN precursor, it is common to obtain other, A-deficient phases together with KNN. $K_4Nb_6O_{17}$, KNb_3O_8 and $K_2Nb_4O_{11}$ have all been reported [35,37,43] and they have a tetragonal tungsten bronze structure. Similar phases containing sodium in place of potassium are also reported, $Na_2Nb_8O_{21}$ and $Na_2Nb_4O_3$ [35]. Due to the stoichiometric similarity in several of the compounds, and of the Na and K atoms, it is often difficult to classify exactly which secondary phase, or combination there of, coexists with the KNN phase. Due to the similarity between the sodium and potassium elements, they likely form together as $(K_{1-x}Na_x)_2Nb_4O_{11}$ rather than as separate phases during KNN synthesis.

By using an excess of alkali metals prior to heat treatment, one can balance out the loss, thereby synthesizing a stoichiometric KNN compound despite the alkali evaporation. Utilizing a pressurized O_2 athmosphere has also been found to successfully mitigate the tendency for K and Na to evaporate, however this approach also yields an increase in conductivity of the final compound. The increase in conductivity originates in the oxygen absorption occurring at high P_{O_2}, resulting in p-type conduction through the compound [44]. A ferroelectric suffering from leakage current is at risk of experiencing complete dielectric breakdown, essentially resulting in a loss of its dielectric, and thus also ferroelectric properties. Mn-doping of KNN has shown to somewhat prevent the increased conductivity stemming from heat treatment in an oxygen rich atmosphere through an increase in valence state. As the compound becomes increasingly oxidized, the Nb^{4+} ions experience an increase in valence to Nb^{5+}. With substituted Mn^{2+} however, a larger increase in valence state is possible, and along with it follows a higher ability to absorb oxygen. As a result, Mn^{2+} becomes oxydized to Mn^{4+} and the compound has a higher resistivity than its undoped counterpart [44]. Leakage current does however also affect thin films synthesized at lower pressures, where alkali metal loss through evaporation is a significant factor, leading to the formation of oxygen vacancies and n-type conduction [45]. It is given then, that the synthesis of high performance KNN thin films is a challenging task, with several factors at opposite ends of the synthesis parameter spectrum that needs to be carefully balanced.

3 Hypothesis

There has been a significant, persistent problem with the work on aqueous solution-based KNN thin film deposition – the formation of secondary phases with composition near $(K_{1-x}Na_x)_2Nb_4O_{11}$ [3, 4]. Many routes were taken in an attempt to eliminate or prevent this phase from forming, with no significant and reproducible results returned. There were however some promising leads, and gaps not yet explored by K. N. Pham. In particular, it was found through EDS STEM analysis that there seems to be an epitaxial layer of the film with an abnormally high Na content. The results illustrating this phenomena for the sample KNNEMn-100-8 – a KNN sample deposited onto STO, with 20 % excess K, Na and 1 % Mn, sintered at 800 °C can be seen in figure 12 [3].

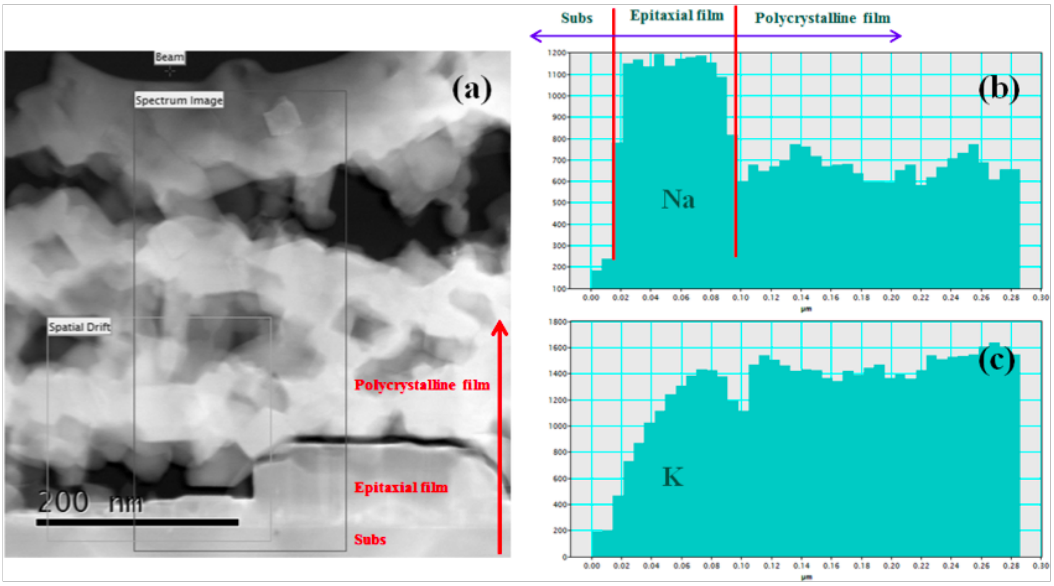

Figure 12: Cross sectional EDS STEM analysis results for the sample KNNEMn-100-8 [3], a 20% excess K, Na KNN sample with a 1% Mn addition deposited onto STO substrate and sintered at 800 °C. (a) STEM image, (b) Na profile, from substrate surface, (c) K profile, from substrate surface.

The origin of the Na-rich epitaxial layer is suspected to be caused by slow, homogeneous nucleation initially occurring at the substrate-film interface. During sintering, a liquid phase is thought to form, supported by the melting points of KNO_3 and $NaNO_3$ at 334 °C and 308 °C respectively [41], forming a growth front which is preferential in favour of sodium, thereby pushing a potassium-niobate rich liquid towards the film surface. With the sodium deficit near the surface, thereby creating an environment rich in niobium in relation to the KNN stoichiometry. With a reduced alkali metal content near the surface,

along with the added possibility of a surface localized deficit due to evaporation, it is expected to facilitate surface growth of the alkali metal-poor, Nb-rich secondary phase; $(K_{1-x}Na_x)_2Nb_4O_{11}$. Successful elimination of the effects of the Na-rich layer then seems to be a likely solution to the problem with constant formation of $(K_{1-x}Na_x)_2Nb_4O_{11}$. This paper will present three different approaches to dealing with the problem, thereby attempting to achieve phase purity:

1. Increase the K and Na content of the solution, performed on SiPt substrates.
2. Deposit an alkali metal-rich solution on top of a sintered sample, performed on SiPt substrates.
3. Increase the pyrolysis temperature, performed on both STO and SiPt substrates.

The first approach aims to allow the formation of the Na-rich epitaxial layer, while ensuring an excess of alkali metals near the surface, thereby allowing the formation of phase pure KNN despite the existence of the epitaxial layer. Both potassium and sodium are known to experience evaporation at higher temperatures [3, 39, 40]. The increased alkali metal approach has previously been attempted on STO substrates [3], but proved unsuccessful at eliminating the secondary phase. However since this paper aims to find a synthesis method suitable for use with SiPt substrates, it is also necessary understand the different behaviours between the two substrates, in order to put the remaining results into context. As such, even if it is not likely to yield successful results on SiPt, it is an important experiment to perform in aiding the general understanding of the other results obtained by K. N. Pham [3]. Furthermore, this route suffers from the potential problem of abnormal grain growth, caused by the additional alkali metal, which becomes intensely volatile at higher temperatures. These grains have shown to yield a reduction in d_{33} values, and as such it is essential to prevent their growth from occurring [42, 46]. This could however turn out to not be the case, should the films grow epitaxially, thereby aligning the grains orientation. The sample relating to this part of the hypothesis is SiPt-400E.

The second approach attempts to create an environment where the existence of KNN on the surface is significantly favoured over that of $(K_{1-x}Na_x)_2Nb_4O_{11}$. By depositing a large amount of alkali metals onto the alkali metal-poor surface and perform heat treatment at 800 °C, the aim is to allow for diffusion of the alkali metals into the $(K_{1-x}Na_x)_2Nb_4O_{11}$ region, and promote a transformation of the latter into the now more stoichiometrically favourable KNN phase. This approach has not been previously tested. A somewhat similar approach was however performed by K. N. Pham on STO substrates, depositing alternate layers of a 20 % excess alkali metal KNN solution and a 1:1 NaCl:KCl solution, with some success in reducing the secondary phase. The sample relating to this part of the hypothesis is SiPt-400alk.

The third and final approach in this paper aims to prevent the formation of the Na-rich layer altogether, by increasing the pyrolysis temperature. This approach promotes homogeneous nucleation in each layer, rather than allowing heterogeneous growth from

the substrate towards the film surface. With the higher temperature and homogeneous growth, it is believed that the Na content will likely remain homogeneous throughout the film, thus allowing stoichiometrically ideal growth conditions in every layer. This approach is also performed on the STO substrates, as K. N. Pham's work did not deal with variations in pyrolysis temperature. Generally, a heterogeneous nucleation of the films is deemed desirable when depositing onto textured substrates, as it allows for more oriented grain growth – the motivation for K. N. Pham to not increase pyrolysis temperature in his work. [3] It is then given that the homogeneous nucleation achievable with higher pyrolysis temperatures can have a negative impact on the films, as one risks somewhat random orientation of the grains – in particular when they form further from the surface, thereby reducing the net total polarization of the films. As the degree of texture in thin films can have a significant effect on the total net polarization [19, 47], this approach may end up yielding subpar performance in comparison to the other two, as the loss caused by the random orientation can be significant, as evidenced by the results achieved by Saito *et. al.* [19]. The samples relating to this part of the hypothesis are STO-450, STO-500, STO-500-2, STO-550, SiPt-500 and SiPt-550.

In addition to the samples necessary for testing the hypothesis, two samples, STO-400 and SiPt-400 were made as to have a good ground for comparison between the effects of the two substrates on the final result. Furthermore, they serve the purpose of drawing a line between the results obtained by K. N. Pham, and those obtained here, thereby allowing a better measure of potential progress in the KNN/secondary phase ratio, as they are both synthesized according to the optimal synthesis parameters obtained in his work.

4 Experimental

4.1 Synthesis

4.1.1 Solutions

0.25 M KNN solutions with 5 % and 20 % excess alkali metal were prepared by mixing of the nitrate compounds of Na and K, a NAmOx solution and deionized water, sol-1 and sol-2. Precursor information is available in table 1.

Precursor	**Formula**	**Purity, [%]**	**Producer**
Potassium nitrate	KNO_3	99.9	Sigma Aldrich, St. Louis, USA
Sodium nitrate	$NaNO_3$	$\leq$ 99.9	Merck, Damstadt, Germany
Ammonium niobate (V) oxylate hydrate (NAmOx)	$(NH_4)NbO(C_2O_4)5H_2O$	99.9	Starck, Goslar, Germany

Table 1: Detailed information regarding the precursors.

The solution used to deposit excess alkali metals as described in the hypothesis chapter, Sol-3, contains alkali metals with a K:N ratio equal to 1:1. A detailed overview of the amounts of precursors in the respective solutions can be found in table 2. All solutions were synthesized using the precursors without further preparation, in the ambient conditions of the fume hood.

NAmOx

The NAmOx solution was synthesized by weighing out 75.568 g of NAmOx powder and stirring thoroughly in 550ml deionized water using a magnetic stirrer, spinning at 300 RPM. The solution was heated to, and held at a constant 70 °C, and covered to avoid excess evaporation. The mixing of the solution was continued for 8 hours and 50 minutes, after which the solution was cooled and calibrated to 0.41 M. Further data regarding the calibration of the NAmOx solution are available in the appendix.

Powders

Powders were made from the KNN solutions in order to ensure that problems relating to phase purity in the films are indeed caused by the synthesis route. KNN powders were synthesized by drying the sol at 80 °C for 24 hours in a lidded platinum crucible. The

Solution	Alkali excess	Precursor	Amount	Concentration
Sol-1	5 %	KNO_3 $NaNO_3$ NAmOx	1.3274 g 1.1159 g 60.2 ml	0.25 M
Sol-2	20 %	KNO_3 $NaNO_3$ NAmOx	1.5166 g 1.2749 g 60.2 ml	0.25 M
Sol-3		KNO_3 $NaNO_3$	1.3271 g 1.1156 g	0.53 M

Table 2: Detailed information regarding the KNN and alkali metal solution contents.

gel was then crushed, and sintering in a lidded silica crucible at 800 °C for 2 hours with a heating rate of 200 °C/h.

4.1.2 Samples

All films were synthesized in an ISO-7 certified clean room, and all solutions were deposited onto the substrates in table 3 using a 0.2 µm filter syringe in order to control the deposited volume and reduce particle contamination in the films. A detailed overview of the sample-specific parameters are available in table 5. A graphical representation of the steps involved in sample preparation is available in figure 13.

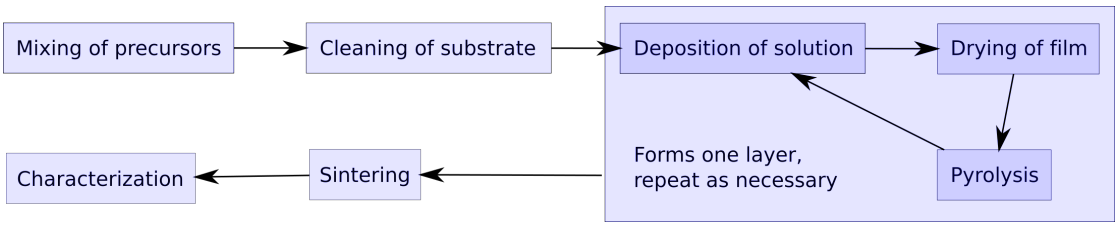

Figure 13: The steps involved in synthesis.

With the exception of SiPt-400alk, every sample was synthesized to have 15 layers deposited upon sintering. SiPt-400alk was initially sintered with 15 layers, as to create a sample with equal synthesis steps as SiPt-400 upon first sintering. Then, sol-3 was deposited onto the sample, and pyrolysis and sintering were performed once more, resulting in a total of 16 layers deposited.

The SiPt substrates consists of a {100} oriented Si bulk, with a {111} oriented Pt surface

Substrate	Orientation	Producer
STO	100	Crystal GmbH
Si	100	MEMS Exchange, Reston, Virginia
Pt	111	

Table 3: Information about the substrates used, and the orientation of their layers.

layer as the face onto which deposition occurs. Between the two layers, there has been observed a thin titanium layer, estimated to 10 nm in width, for which the direction of orientation, if any, is uncertain. The STO substrates are cut as to provide a {100} surface for deposition, and contain no other layers or elements.

Substrate cleaning procedures

Before deposition, the substrates were cleaned. Piranha etching or oxygen plasma were used to ensure clean, oxygenated substrate surfaces. Piranha etching was performed for 18-23 minutes, with a median 21 minutes, and a 3:1 H_2SO_4:H_2O_2 ratio of the precursors, with concentrations as per table 4. After etching, the samples were rinsed twice for 2 minutes in deionized water and dried with N5.0 grade N_2 gas. The time between etching and the first deposited layer ranges from less than one week to two months.

Precursor	Formula	Concentration, [%]	Producer
Sulfuric acid	H_2SO_4	95-98	Merck KGaA, Damstadt, Germany
Hydrogen peroxide	H_2O_2	30	Merck KGaA, Damstadt, Germany

Table 4: Detailed information regarding precursors for the piranha solution.

Plasma cleaning was performed in a diener Femto using O_2 plasma with 50% power and flow rate for 1 minute. The samples cleaned with oxygen plasma were coated within 20 minutes of cleaning. Detailed overview of which cleaning procedures were used for which samples can be found in table 5.

Deposition

Spin coating was chosen as the method of depositing the solution onto the substrates. The spin coater used was the Laurell model WS-400B-6NPP/LITE/AS. The initial layer

of each sample was deposited using 0.9 ml of solution, while subsequent layers received 0.6 ml of solution. Spin coating was performed at 3000 RPM for 35 seconds, including a run-up time of 5 seconds, according to the method developed by K. N. Pham [3].

4.1.3 Heat treatment

Upon completion of spin coating, the samples were dried on a Heidolph MR 3001 magnetic stirring hot plate at 150 °C for 2-3 minutes, ensuring complete evaporation of the liquid, thereby better preventing contamination of the film prior to pyrolysis, while also ensuring the film quality did not deteriorate due to solution agglomeration. Following the removal of a visibly high quality film from the hot plate, the samples were pyrolyzed for 5 minutes at temperatures as per table 5. Upon reaching the desired number of layers, the films were sintered at 800 °C for 10 minutes, according to the results obtained by K. N. Pham [3].

Hypothesis route	**Sample**	**Solution**	**Pyrolysis T, [°C]**	**Cleaning method**
Control	SiPt-400 STO-400	1	400	Piranha
1	SiPt-400E	2	400	Piranha
2	SiPt-400alk	1, 3	400	Piranha
3	STO-450	1	450	Piranha
	STO-500		500	
3	STO-500-2	1	500	O_2 Plasma
	SiPt-500			
	STO-550		550	
	SiPt-550			
	SiPt-500P	1	500	O_2 Plasma

Table 5: Detailed information regarding the individual sample variables, grouped according to hypothesis path. The SiPt-500P sample has not been sintered, and coated with 6 layers, as opposed to the 15 layers on all other samples.

Both pyrolysis and sintering were performed using a silicon carbide susceptor as per

figure 14 in a rapid thermal processing oven, the JIPELEC JetFirst 200, with a constant O_2 gas supply of 100 sccm and a heating rate of 25-27 °C/s. In addition to the samples, the susceptor also contained sacrificial KNN powder as per figure 14 [3], in an attempt to nullify the effects of alkali metal evaporation [40] during pyrolysis, and in particular during sintering.

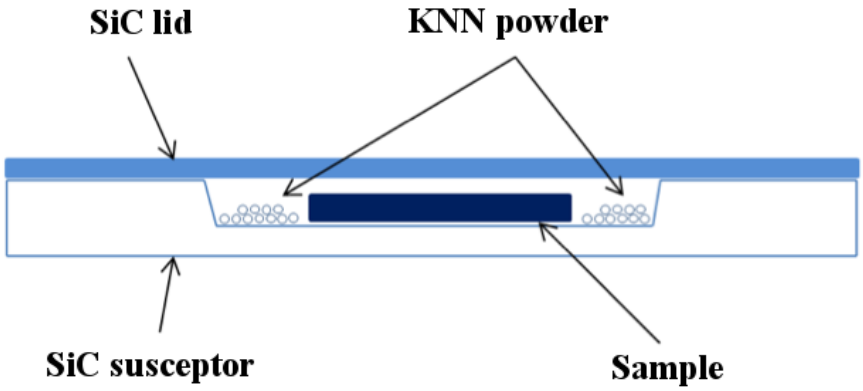

Figure 14: Illustration of the susceptor, sample position and sacrificial powder used during heat treatment in the RTP oven.

4.2 Characterization

4.2.1 X-ray diffraction analysis

Using XRD for sample analysis is preferable to GIXRD, as it provides better information, especially concerning epitaxy and orientation. However, due to the strong signal from the substrates in the relevant regions, it is not suitable for the samples in this paper in terms of general analysis, as both substrates are oriented at their surface, according to table 3. The STO substrate has peaks at 23°and 46°, while the SiPt substrate has a peak from the platinum layer centred around 40°, all of which interfere with proper analysis of the data due to their width and hence overlap with several peaks from both the KNN and secondary phases. As such, grazing incidence has been chosen as the preferred setup for XRD analysis.

Grazing incidence XRD

The samples were analyzed primarily using a grazing incidence (GI) setup on a Bruker D8-DaVinci with 2° incidence angle. This setup was chosen as it provides a sufficient penetration depth of the films, while simultaneously preventing signal from the substrate, thus maximizing the signal-to-noise ratio. The Bruker D8-DaVinci utilizes Cu-Kα radiation with a wavelength of 1.54056 Å. A scanning speed of 4 s/step was used, with a step size of 0.3°.

One sample deposited onto a SiPt substrate, SiPt-500-6, with 6 layers of sol-1 and pyrolyzed at 500 °C was analyzed prior to sintering, in order to better understand the effects of sintering on morphology and phase formation. During analysis of this specific sample, a 0.40 mm Soller's slit was used, as the signal-to-noise ratio is otherwise insufficient with respect to the certainty of the results obtained due to the reduced thickness of the film.

For all other samples, a 0.25 mm Soller's slit was used.

XRD

The samples SiPt-400, SiPt-500, STO-400 and STO-550, along with their respective clean substrates were further analyzed with a Bragg-Brentano configuration. Due to the textured nature of the substrates, it is not possible to sufficiently analyze the samples through GIXRD alone when textured growth is suspected. The scans were performed using a Ni-filter as well as a Pb-slit on the incoming beam, in order to lessen the signal from the substrates as well as edge defects of the samples, thereby only gathering signal from the central 0.6mm^2 sample area. These scans were performed with a scanning time of 2.4s/step and a step size of 0.027°.

The KNN powders from sol-1 and sol-2, as described under the solutions – powders chapter, were analyzed using a scanning time of 0.8 s/step with step size 0.013°.

4.2.2 SEM – EDS

SEM has been used for selected samples only, as the main purpose is to achieve phase purity. SEM was used to analyse the morphology and compositional homogeneity of the samples. Primarily the film surface, but also cross sectional analysis when appropriate, based on XRD results. As the films are in the range of 300 nm, a relatively low acceleration voltage was used, ranging from 3 kV to 10 kV. EDS analysis was also performed, but were mostly supplemental in nature, due to the resolution possible with the technique in relation to the requirements originating in the sample size. For EDS analysis, an accelerating voltage of 15 kV was used, as it was deemed necessary in order to improve the signal strength.

For cross section analysis, the samples were cut in half using a glass cutter, without further preparations in terms of polishing etc, thereby leaving the fracture surface untouched. By further preparing the surface for SEM analysis through polishing, there is an inherent risk of damaging the surface, or causing pull-out from the substrate or film, which could prevent proper analysis. When leaving the fracture surface untouched, the cross section may present morphology otherwise difficult to analyze, even if the quality may be lower due to the potentially rough fracture surface.

Due to the dielectric nature of the films, sample preparation is necessary in order to perform SEM or EDS analysis. For surface analysis, the samples were wrapped in aluminium foil, leaving only the central film area uncovered. Carbon tape was used

to ensure proper conduction between the samples and sample holder. Cross sectional analysis did not use aluminium foil, but rather just carbon taping of the samples to the sample holder, as this was found to be sufficient. SEM analysis was performed using the LVFESEM Zeiss Supra 55VP, equipped with the EDAX Octane Pro for EDS.

5 Results

5.1 Synthesis

5.1.1 Solutions

The solutions used, including the NAmOx solution, has been found to remain stable over time in terms of precipitation, deposited layer quality as well as final sample quality, with solution age near 4 months. There are non-dissolved contaminants slightly visible during stirring of the solutions, which are assumed to be caused by dust particles from the ambient conditions of the fume hoods in the laboratory used to prepare the solution. The particles are successfully filtered out prior to deposition with the use of the syringe equipped with a 0.2 µm filter.

The nitrate precursors were not dried prior to measuring. It was expected to have negligible impact on the accuracy of the final stoichiometry, since a significant excess is used in all solutions and the equipment used for heat treatment does not allow for collection of data relating to alkali metal evaporation, preventing more accurate solution stoichiometry. It then follows that the solutions are likely to contain slightly below reported values of excess alkali metals.

XRD scans of KNN powders synthesized from sol-1 and sol-2 are available in figure 15. The solutions were both found to yield satisfactory results during powder synthesis, and problems relating to phase purity during thin film synthesis are indeed deemed to be caused by the synthesis route, and not the solutions or precursors, hence no further attempts were made in order to more accurately calibrate the solutions used. The excess alkali metal is assumed to evaporate during sintering.

There is clear peak splitting visible in the XRD analysis results of the KNN powders, as is expected for an orthorhombic structure [48].

5.1.2 Substrate wettability

Piranha etching was found to significantly increase the wettability of both substrates used, STO slightly more so than SiPt. It was noted that there was gas formation on the Pt side of the SiPt substrates, with the Pt surface layer likely acting as a catalyst. This phenomenon was not visible on the STO substrates. As a result of the gas formation, the SiPt substrates were often found in the piranha - air interface, hence not fully immersed in the solution, which could lead to an insufficiently homogeneous or incomplete etching of the substrates. Due to the median time spent in the solution however, it is likely not a significant factor when judging the overall success of the process.

Immediately after completion of the etching, complete wetting of the substrates with very low contact angles was achieved, using deionized water. The wettability did, however

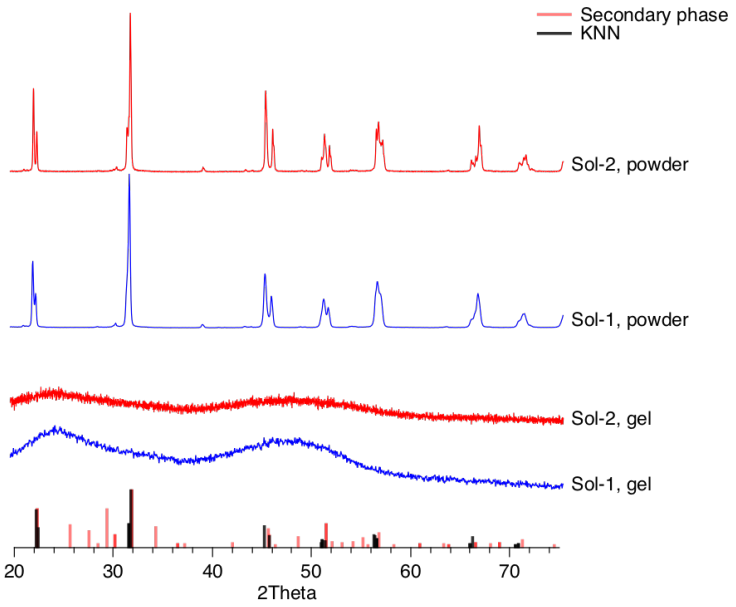

Figure 15: XRD scans with Bragg-Brentano configuration for the KNN powders and gels synthesized from sol-1 and sol-2, as marked by the legends. Indexed according to pdf patterns 040170216 and 040108978 for the KNN and $K_2Nb_4O_{11}$ phases, respectively. For the purpose of presentation, the XRD results are not plotted to scale.

deteriorate over a time span of two months, and eventually, proper wetting could no longer be achieved. To alleviate this problem of poor wettability, an attempt was made to form a thick layer of gel by depositing solution onto the substrates while they were heated up using the hot plate, to force rapid evaporation of the solution and homogeneous gel formation. The gel would then be cleaned off of the substrates by dissolving it in water, returning to a visibly clean substrate. This procedure was attempted on STO-500. Despite achieving excellent wetting between the substrate and deposited solution, the procedure was found to likely have a negative impact on the morphological homogeneity, resulting in porosities as evidenced by SEM analysis, figure 16. Due to the negative impact on sample quality, there was no further investigation into whether or not this method has any effect on the formation of the $(K_{1-x}Na_x)_2Nb_4O_{11}$ phase, or if it is limited to morphology.

As the effect of piranha etching was found to deteriorate over time, and the attempts made to achieve better wetting were deemed unsuitable, the use of piranha etching was replaced by oxygen plasma cleaning. The wetting achieved was found to be excellent regardless of substrate. Due to the simplicity of the procedure, the substrates were cleaned immediately prior to use. As such, the longevity of the oxygen layer was not investigated further.

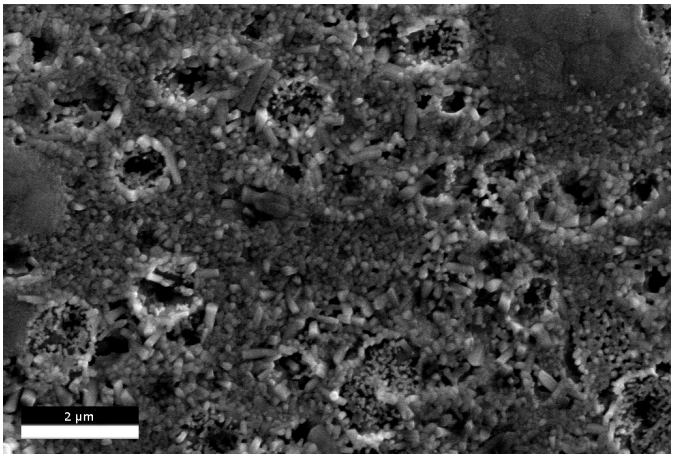

Figure 16: SEM image of the STO-500 sample.

5.1.3 Hot plate temperature

K. N. Pham [3] found a hot plate temperature of 200 °C to be suitable. This temperature, however, was found to cause excessive boiling of the solution during experimentation with gel formation prior to deposition in an attempt to increase wettability. The excessive boiling also resulted in the formation of large bubbles in the gel. As this work focuses on a PVA-free solution, the need for a higher temperature is reduced. By reducing the temperature of the hot plate to 150 °C, the gel becomes more homogeneous by preventing the formation of large bubbles. Its impact on synthesis time is negligible as the amount of solution deposited is minimal, and gel formation occurs at both temperatures within 2 minutes. As the quality of the formed gel layer is visibly higher, it could potentially have a positive impact on the quality of the post-pyrolysis layer, allowing for a more homogeneous morphology in the sintered sample by allowing improved growth conditions in succeeding layers.

5.1.4 Deposition quality

Spin coating as a means of deposition was found to be a very simple and efficient way to deposit the solution. There were some problems relating to consistency of the film quality, but the relevant parameters have not been fully identified. The problems were primarily experienced during deposition of the primary layer onto the substrate, and not when depositing onto a previously deposited layer. The origin of the inconsistencies are uncertain, but found to be affected by at least the mounting position of the substrate and possibly also the spin-up period, which resulted in an uneven layer thickness. Continuation of the synthesis upon deposition of such a layer has been found to further propagate the phenomenon.

The deposited layer can be observed through fluorescence to change rapidly during spin coating, in a period of up to 20-25 seconds. The samples have been found to experience some densification during pyrolysis while maintaining a consistent thickness, observed through fluorescence. Sample thickness has also been investigated by means of cross sectional SEM analysis, discussed in more detail in the SEM chapter. Based on the results, the current spin coating time is considered suitable given the RPM utilized.

5.2 Sample characterization

5.2.1 Grazing incidence XRD analysis

All samples were analyzed by means of grazing incidence. The GIXRD results for samples relating to the hypothesis paths attempting to prevent the Na deficiency by focusing on the local stoichiometry are found in figure 17a. Additionally, the samples made for comparative reasons, SiPt-400 and STO-400, are also found in this figure. The results for the samples focusing on temperature and nucleation are found in figure 17b.

As there is an overlap between the two phases on the important KNN peaks, it is not possible to judge progress by considering the peak in question. Rather, it is necessary to consider the intensity of the main KNN peaks against that of the separate secondary phase peaks. It is clear then, that the change obtained for the SiPt-400E is in line with expectations based on the works with STO by K. N. Pham [3]. Furthermore, the SiPt-400alk sample shows no significant changes when comparing the scans taken prior to, and after deposition of sol-3, as well as no significant changes in comparison to the SiPt-400 sample. It is clear then that neither the 20% excess alkali metal solution or the deposition of an alkali metal-rich solution on top followed by diffusion into the top layers during sintering are successful in significantly changing the ratio between the KNN and secondary phases.

For the temperature-based approach however, there is a clear drop in the reflections corresponding to $(K_{1-x}Na_x)_2Nb_4O_{11}$ only, while the KNN reflections remain with strong for the samples pyrolyzed at $T = 500\,^{\circ}\mathrm{C}$. Figure 18 shows, through sample STO-500-2, that the improved ratios obtained in STO-500 from figure 17b are repeatable, and can be further improved upon. Also visible for the high temperature STO-based samples, is the beginning of orthorhombic peak splitting.

The intensity ratios seem to improve somewhat when raising the temperature further, to $550\,^{\circ}\mathrm{C}$. Furthermore, it is clear the the significantly improved ratios achieved with the STO substrates are indeed transferable to SiPt, although with a comparatively reduced $\mathrm{KNN}/(K_{1-x}Na_x)_2Nb_4O_{11}$ ratio.

The SiPt-500P sample was analyzed to better understand the origin of the improvements seen in the samples sintered at $T \geq 500\,^{\circ}\mathrm{C}$. It is clear that the KNN phase forms at least partially prior to sintering, as the phase can be indexed in the scan for the sample in figure 19.

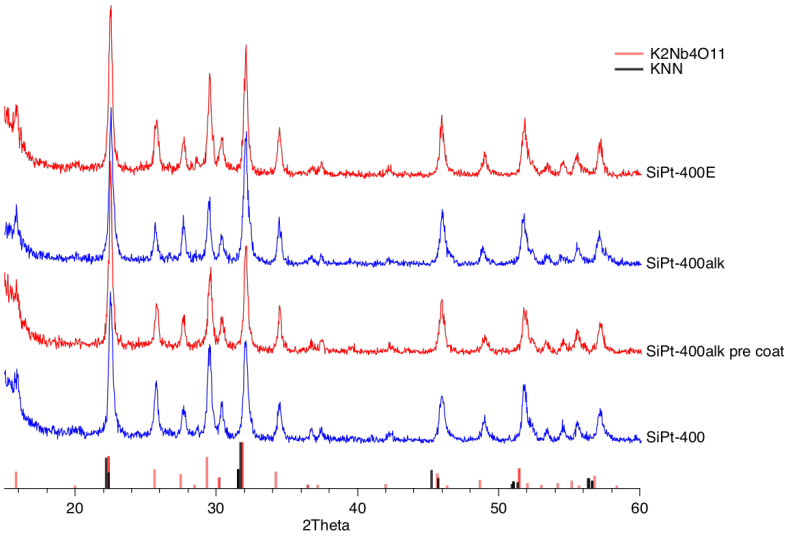

(a) Grazing incidence results from samples synthesized with 5% (SiPt-400) and 20% (SiPt-400E) excess alkali metal and sample with extra alkali metals deposited post-sintering (SiPt-400alk).

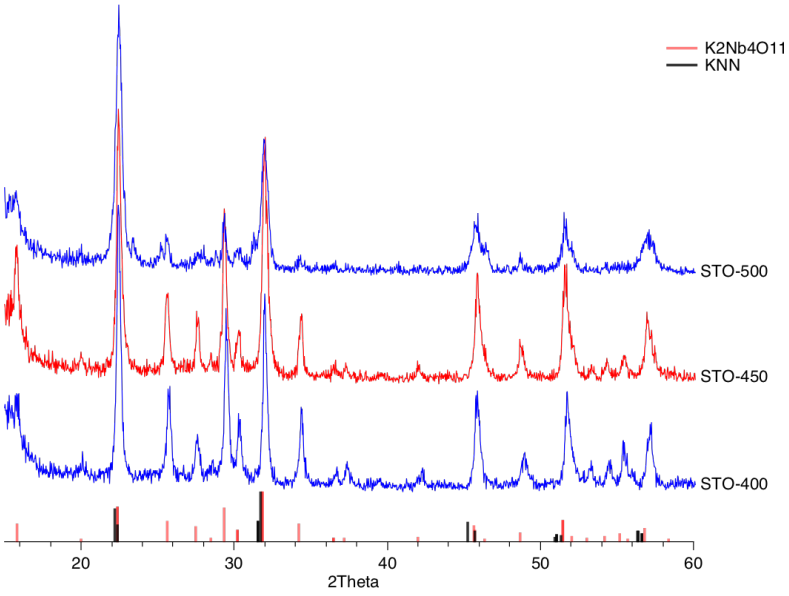

(b) Grazing incidence results from samples synthesized with varying pyrolysis temperatures.

Figure 17: Samples in (a) are part of the first and second, alkali metal-deficient hypotheses, (b) contains samples relating to the third temperature-based hypothesis. Indexed according to pdf patterns 040170216 and 040108978 for the KNN and $K_2Nb_4O_{11}$ phases, respectively. All plots in this figure are plotted to relative scale.

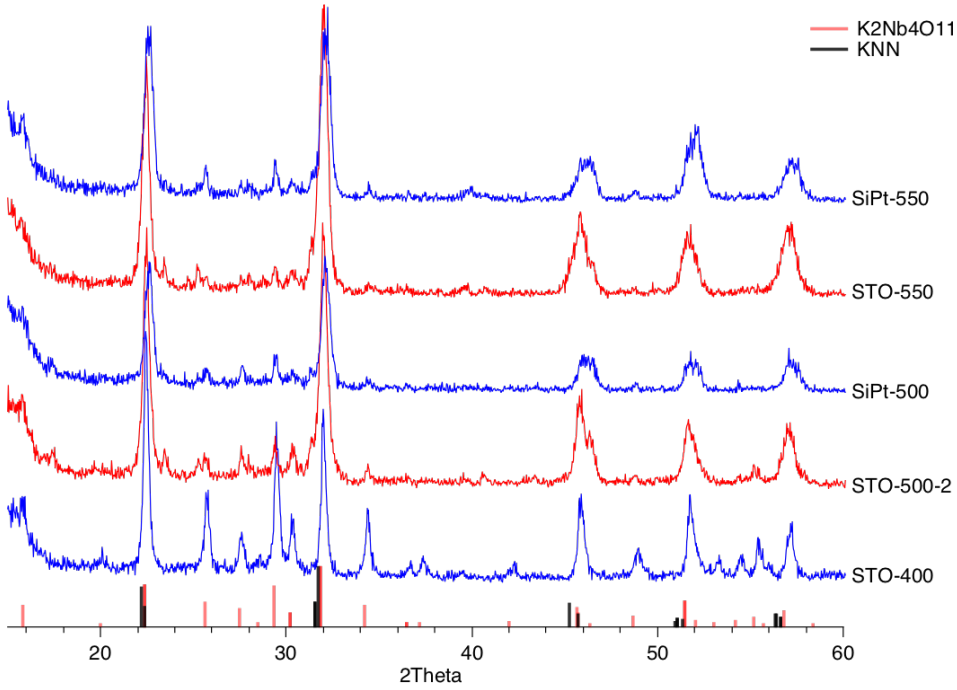

Figure 18: Samples plotted are attempted reproduction of STO-500, in STO-500-2, as well as experiments to establish the effects of further increases in temperature. Additionally, the high temperature pyrolysis is attempted on SiPt substrates, to see whether the results are transferable, or substrate-limited. Indexed according to pdf patterns 040170216 and 040108978 for the KNN and $K_2Nb_4O_{11}$ phases, respectively. All plots in this figure are plotted to relative scale.

There are also signs of the $(K_{1-x}Na_x)_2Nb_4O_{11}$ phase, but due to the noise in the data, it is difficult to conclude whether the phase has formed or if the signal is primarily background signal – and if formed, the degree of formation in relation to KNN, in comparison to the post-sintering results.

5.2.2 XRD analysis

As the substrates are textured, further analysis of a subset of the samples showing significant improvements were done using Bragg-Brentano configured XRD. The XRD analysis will show whether the films have grown with a preference in orientation or epitaxially. The results for the SiPt-based samples are available in figure 20a, while figure 20b shows the results from the STO-based samples.

The scans are performed using a Ni-filter, and a Pb-slit, to block the incoming beam and absorb secondary radiation, thereby minimizing the signal obtained from the substrate and potential edge defects in the film. The sharp peak also visible on the clean substrates

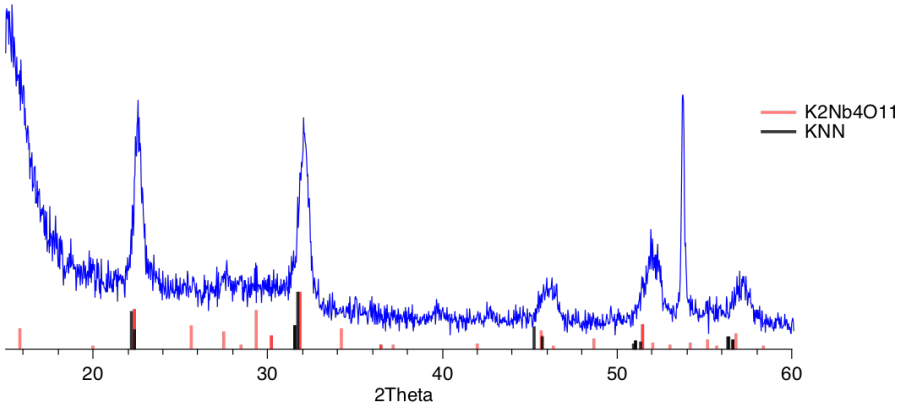

Figure 19: SiPt-based sample pyrolyzed at 500 °C, with 6 layers of sol-1 deposited. Sample is not sintered. GIXRD scan is performed using a 0.40mm Soller's slit for increased intensity. Indexed according to pdf patterns 040170216 and 040108978 for the KNN and $K_2Nb_4O_{11}$ phases, respectively. All plots in this figure are plotted to relative scale.

at 31° and 42° respectively, for SiPt and STO is caused by the incomplete absorption of the radiation by the Ni-filter around the substrate peak.

Samples based on both substrates show a clear shift in their KNN/secondary phase ratios in favour of KNN with the increase in temperature. However, as the temperature increases, favouring homogeneous nucleation, it seems that the degree of epitaxy is indeed decreased. This is most notable when comparing the KNN reflections centred around 22° and 32° on the SiPt-based samples, as there is overlap between the KNN reflection at 22° and the STO substrate reflection. A clear shift in intensities between the two reflections occur when increasing the temperature from 400 °C to 500 °C, moving towards the indexed patterns. There is however likely still some degree of preferred orientation in the high temperature samples.

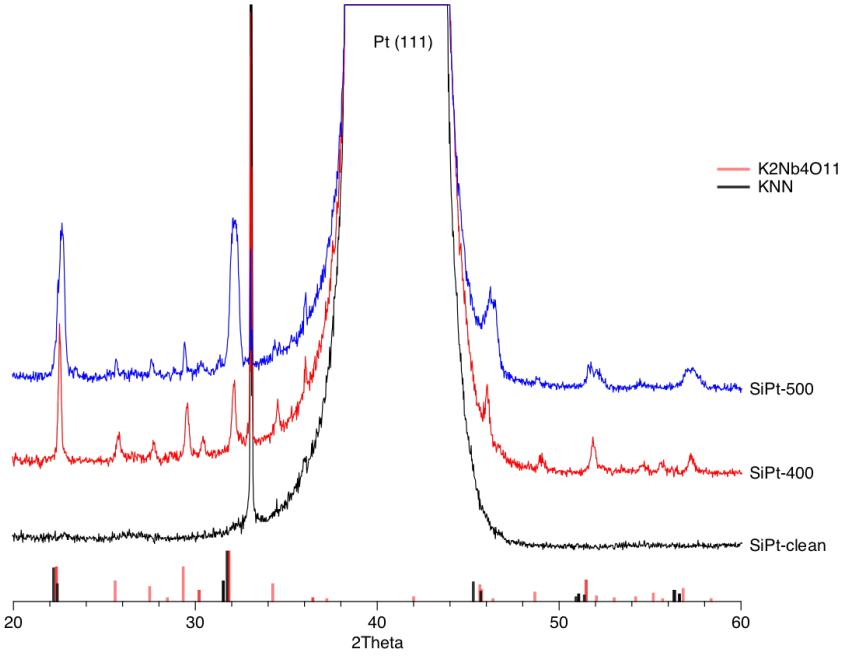

(a) XRD scans of the SiPt-400 and SiPt-500 samples, as well as the clean SiPt substrate.

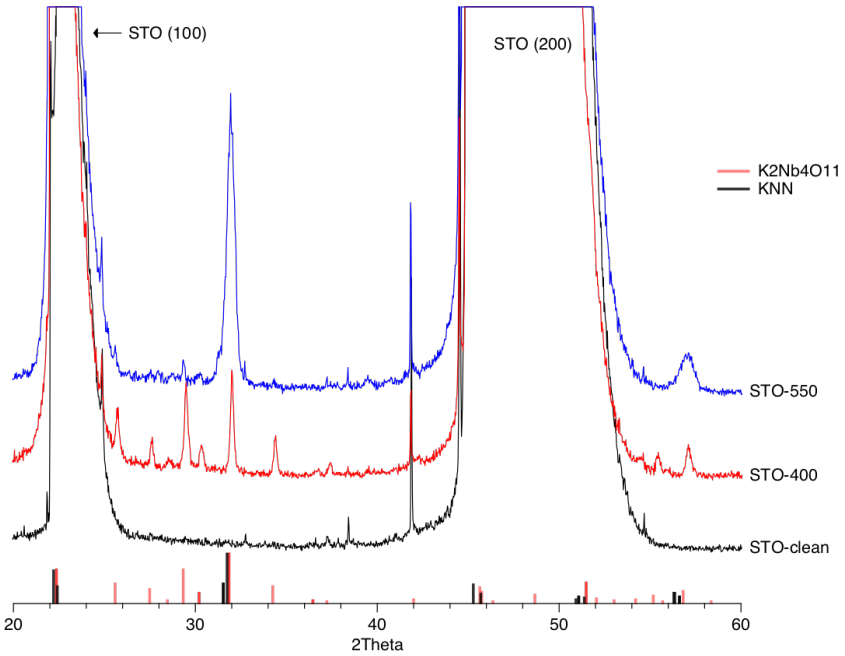

(b) XRD scans of the STO-400 and STO-550 samples, as well as the clean STO substrate.

Figure 20: The scans are performed using a Ni-filter, and a Pb-slit. Indexed according to pdf patterns 040170216 and 040108978 for the KNN and $K_2Nb_4O_{11}$ phases, respectively.

5.2.3 SEM surface analysis

It is evident that the phase $(K_{1-x}Na_x)_2Nb_4O_{11}$ is still present on the surface, visible as the needle or plate-like grains in figure 21c. These grains were also observed in previous works [3, 4], and their presence is expected given the XRD results. Figure 21c does however show that their coverage of the surface is not complete, possibly correlated with the reduction of $(K_{1-x}Na_x)_2Nb_4O_{11}$ seen in the XRD results.

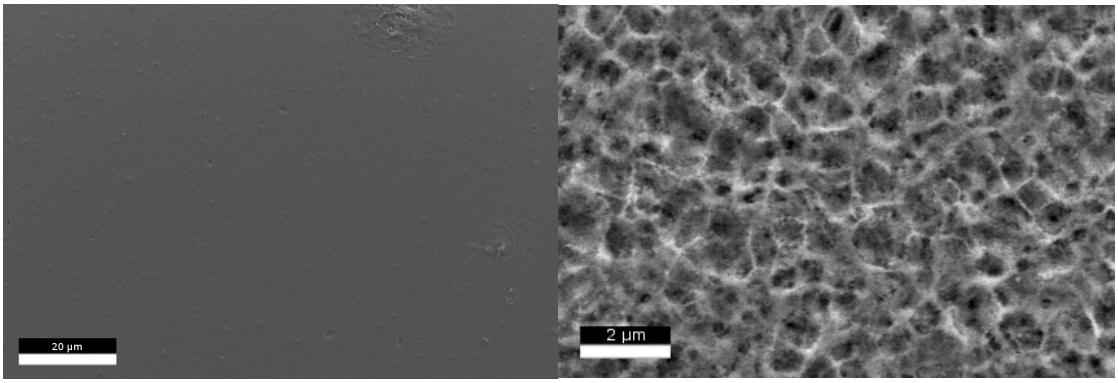

(a) SEM image of the surface of sample STO-500-2.

(b) SEM image of the surface of sample STO-400.

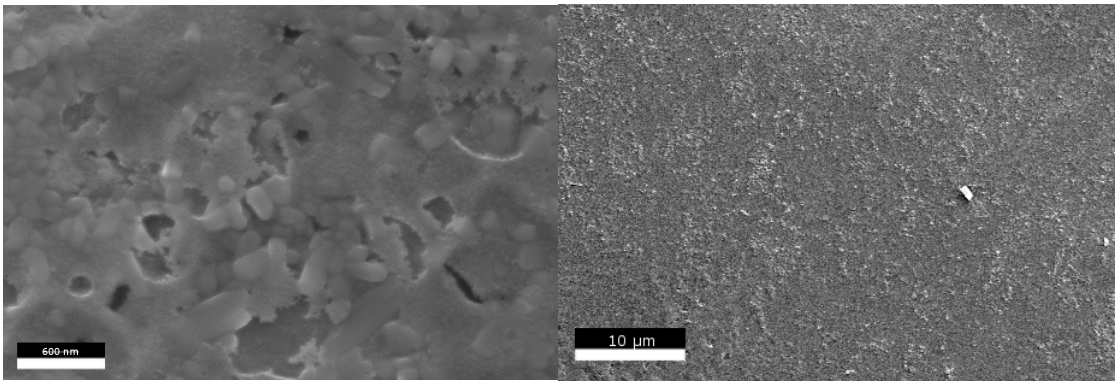

(c) SEM image of the surface morphology of sample STO-550.

(d) SEM image of sample made by K. N. Pham.

Figure 21: (c) SEM image of the surface morphology of sample STO-550. Despite even surface and progress made in phase ratios, the $(K_{1-x}Na_x)_2Nb_4O_{11}$ phase is still visible on the surface, recognized by its morphologically distinct elongated grains. (d) SEM image of the surface morphology of a {100} STO sample made by K. N. Pham, in accordance with his synthesis method [3].

The surface of STO-500-2, figure 21a, is morphologically even, and free of larger defects and pores, and the improvements can likely be attributed to the improved wetting

achieved with O_2 plasma in comparison to that offered by aged piranha etched substrates. The morphological improvements of STO-500-2, in comparison to STO-400, figure 21b, are evident. Furthermore, the morphology achieved with STO-500-2 shows improvements over that achieved by K. N. Pham, figure 21d [49].

5.2.4 SEM, cross section analysis

Cross section analysis was performed on the SiPt-400, SiPt-500 and STO-550 samples, in order to understand the phenomena responsible for the reduction in $(K_{1-x}Na_x)_2Nb_4O_{11}$ and the formation of KNN prior to sintering. Sample thickness is found to be even for all samples analyzed, in the vicinity of 300nm.

The SiPt-400 sample presents with evenly sized grains throughout the sample, but without visible signs of epitaxial growth, figure 22a. Also visible, is the platinum and titanium layers between the film and the bulk silicon substrate.

SiPt-500 however, figure 22c, shows clear signs of epitaxial growth, despite a higher pyrolysis temperature. Furthermore, the grain growth has been significant in this sample, and seemingly of monocrystalline nature, starting at the substrate-film interface and growing towards the film surface. The grain growth is however not complete, which leaves very fine nanograins in the surface region – visible in figure 21c.

As evidenced by figure 22b, similar crystal growth has taken place in the STO-550 sample; also presenting with significant, seemingly epitaxial grain growth. Unlike SiPt-500 however, the grain growth is mostly completed, with few nanosized surface grains remaining. It does however seem epitaxial only in the vicinity of the substrate, and loses its preference for orientation near the surface of the film. It is difficult to say if this is supported by the XRD results in figure 20b and 20a, as one of the main reflections for KNN is covered by the {100} reflection from the STO substrate. The remaining reflection peaks are of comparably insignificant intensity, making it difficult to draw meaningful conclusions with basis in them.

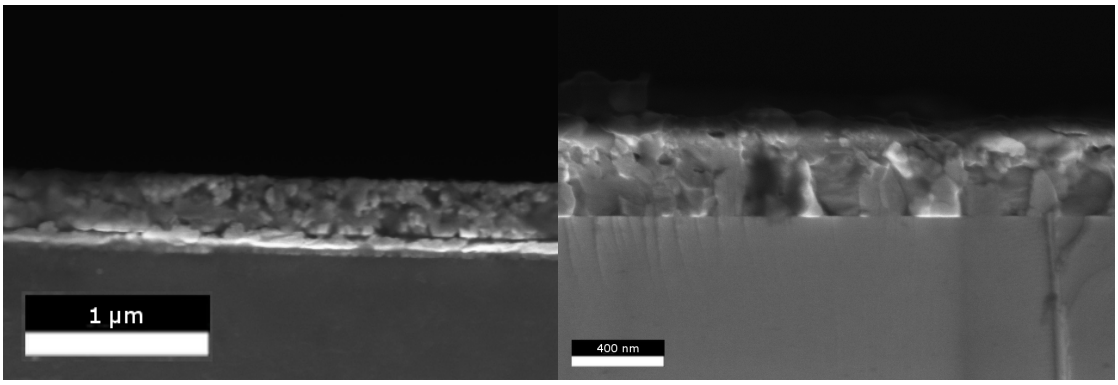

(a) Cross-sectional SEM image of the sample SiPt-400.

(b) Cross-sectional SEM image of the STO-550 sample.

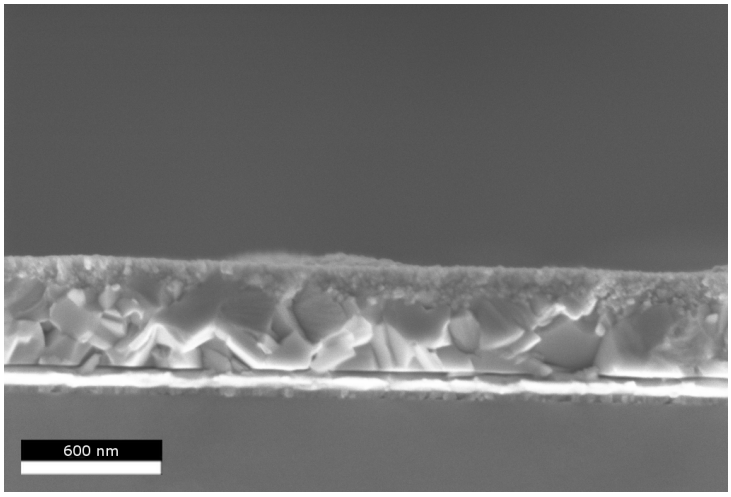

(c) Cross-sectional SEM image of the SiPt-500 sample.

Figure 22: Cross sectional SEM images, showing seemingly (a) randomly grown crystals, and (b+c) epitaxial somewhat monocrystalline growth, partially and fully completed, for (b) and (c) respectively.

EDS

The analysis of SiPt-500 was further supplemented with EDS of the cross section, primarily to confirm element homogeneity throughout the sample. Due to the poor signal strength, it is difficult to accurately judge whether there is an epitaxial Na-rich region, however figure 23b, 23c show that there is likely no concentration gradient in the film when pyrolysis is performed at 500 °C. If the sodium-rich epitaxial layer is indeed present in the sample, then it is likely as part of $NaNbO_3$ or other, similarly niobium-rich phases, as the niobium is homogeneously distributed throughout the sample, figure 23d – and is not significantly affected by the pyrolysis within the temperature range used. EDS results obtained for SiPt-400 mirror those obtained for SiPt-500, but with inferior quality. As such, the decision to only report one set of results was made.

Furthermore, the EDS analysis does confirm that the SiPt substrate is indeed composed with an interstitial titanium layer between the silicon bulk and platinum surface layer, as per figure 23d-f.

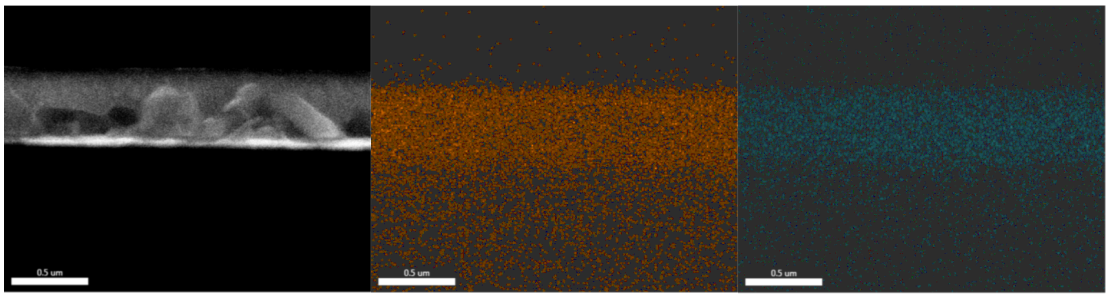

(a) Cross section SEM image of SiPt-500.

(b) Element mapping of Na in SiPt-500.

(c) Element mapping of K in SiPt-500.

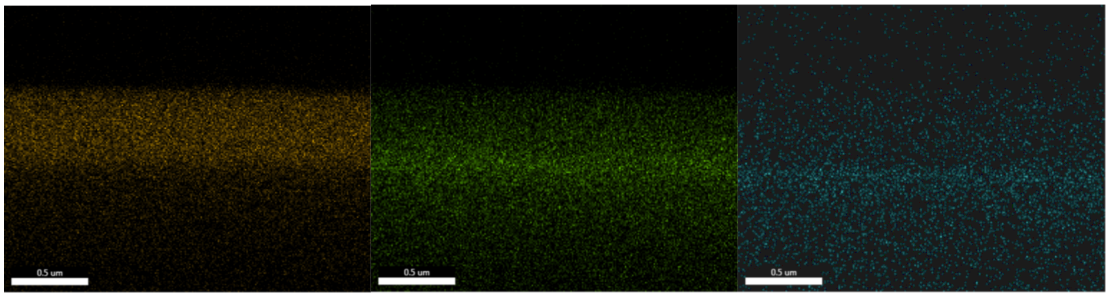

(d) Element mapping of Nb in SiPt-500.

(e) Element mapping of Pt in SiPt-500.

(f) Element mapping of Ti in SiPt-500.

Figure 23: Cross-sectional element mapping of sample SiPt-500. Saturation of (b), (c) and (f) has been increased for presentation purposes.

6 Discussion

6.1 Synthesis

All samples were synthesized in a susceptor with a small crack, thus increasing the gas flow inside the susceptor, allowing it to more closely mirror that of the RTP chamber. The cause of the crack in the susceptor is thought to be related to the temperature of the gas flowing into the chamber in the RTP. The gas is not heated prior to entering the chamber, and seems to hit the susceptor thereby causing a significant, crack-inducing temperature gradient. As a result, it is likely that the temperature experienced by the samples does not exactly match that of the reading thermocouple in the chamber, as the calibration environment is not the same as that used during heat treatment – hence their degree of correspondence with that reported in literature may not be accurate. As such, the significant shift in KNN/secondary phase ratio could occur at a slightly different temperature than that reported in these and other works.

While the results obtained by K. N. Pham [3] suggest that 800 °C is the optimal sintering temperature in terms of piezoelectric properties, the $K_2Nb_4O_{11}$ phase and similar compounds have been reported forming in favour of KNN with increasing temperatures from 800 °C and upwards [43, 50]. It can be argued that the improved results obtained by increasing the sintering temperature from 700 °C to 800 °C are linked to the increase in KNN phase formation, as the pyrolysis temperature is not sufficient to promote KNN crystallization – hence 800 °C may not necessarily be preferable to 700 °C, provided a sufficiently high pyrolysis temperature.

The sol-gel method has been known to cause cracks when combined with thin film synthesis [51]. However, no sign of significant cracks have been observed within the current parameters, suggesting an increase in film thickness is possible without an immediate deterioration of film quality.

6.2 Characterization

6.2.1 SEM – XRD

As evidenced by figure 22c, there seems to be significant grain growth occurring primarily during sintering in SiPt-500, which could be a result of the excess alkali metal in the solutions; this suggests the existence of a liquid phase during sintering [42]. As the sintering temperature remains static in all samples, it is reasonable to expect the liquid phase sintering to occur in all samples and not limited to the ones also undergoing pyrolysis at $T \geq 500$ °C. The grain growth, especially due to the its epitaxial nature as observed in SiPt-500, could prove to be beneficial by causing an increase in piezoelectric properties [52]. The correlation between grain size and piezoelectric properties is further supported by research done on the PZT system [53].

It has been found that KNN films annealed at 550 °C show a significant degree of texture caused by the crystallization of KNN around this temperature [50, 54, 55], whereas films annealed at a lower temperature instead present with a somewhat random orientation of the grains [55]. This report conforms with the results obtained here, showing no preferential orientation at 400 °C, but significant preferential orientation starting from 500 °C – caused by the annealing of the film and crystal growth after each layer deposition. Furthermore, it entails that there is no crystallization of KNN prior to sintering in the films pyrolyzed at 400 °C, hence little epitaxial KNN grain growth, and that the nucleation would first start during sintering and be homogeneous – both of which seem plausible based on the cross section analysis of the SiPt-400 sample in figure 22a.

The SiPt-500 sample however, shows nucleation in the top-most layers and significant preferential orientation of the larger grains originating in the substrate. This could be the result of a kinetically delayed growth rate in comparison to layer thickness and pyrolysis time. Combined with an inefficient growth direction, it can be argued that the grains located in the surface region are indeed growing individually, but eventually contribute the growth of the larger, epitaxial grains.

It is observed that the STO-550 sample has complete, textured grain growth, while it presents as incomplete in SiPt-500. This is likely linked to temperature increasing the growth rate, however, could also be attributed to the angle at which the growth occurs on the {111} substrates, where the grains impinge on each other, effectively limiting the growth rate of neighbouring grains. On {100} oriented substrates however, the growth occurs perpendicular to the substrate, effectively providing a shorter growth distance to the surface and eliminates the impingement of neighbouring grains. Further comparative analysis of the SiPt-550 and STO-500 samples would be necessary in order to determine whether this calls for differing holding times of the {100} and {111} oriented substrates, and potentially also an increased alkali metal-excess in the {111} based-samples in comparison to those deposited onto {100} substrates.

As the KNN formation is reported to occur around 550 °C, and in this report also observed at 500 °C, it could be that the formation of $(K_{1-x}Na_x)_2Nb_4O_{11}$ does not in fact occur preferentially at the surface in favour of KNN. Rather, when the KNN does form during sintering for samples pyrolyzed at 400 °C, there is preexisting $(K_{1-x}Na_x)_2Nb_4O_{11}$. The $(K_{1-x}Na_x)_2Nb_4O_{11}$ may then only partially transform into KNN, limited by kinetics and alkali metal-evaporation in the region. As such, an increased sintering time could also be considered, to allow for a complete transformation of the $(K_{1-x}Na_x)_2Nb_4O_{11}$ phase. Raising the sintering time to improve the kinetics however, is not recommended as it has been shown to promote the growth of $(K_{1-x}Na_x)_2Nb_4O_{11}$, likely due to evaporation of alkali metals [3, 50]. This has also been observed through variations in sintering temperature [50], and can likely be linked to the lack of excess alkali metals in the solution used. It does not account for alkali metal evaporation, and is likely to stoichiometrically limit the KNN formation by creating an A-deficient growth environment.

6.3 Hypothesis

Given the results obtained, it is clear that the attempted elimination of the $(K_{1-x}Na_x)_2Nb_4O_{11}$ phase in samples pyrolyzed at 400 °C has been unsuccessful, regardless of other synthesis parameters. It seems that the addition of excess alkali metal becomes increasingly necessary with an increase in temperatures and holding times [50]. However, there is currently little reason to believe that an excess beyond 5 % is the missing piece on the road to phase purity, as the samples pyrolyzed at $T \geq 500$ °C show continuous improvements with increasing temperatures. Changes to the A-stoichiometry, increasing the potassium content in favour of sodium, has however been found to further improve the ferroelectric properties in comparison to films synthesized using a 1:1 K:Na stoichiometry [55].

The $T \geq 500$ °C samples show some promising results, likely linked to the subsequent KNN formation after each deposited layer. It has been reported by thermal analysis for synthesis of KNN nano particles and thin films through a sol-gel approach that the lowest temperature necessary to obtain powders of KNN is in the region 550-600 °C [54, 55]. There is then some merit to the idea of further increasing the pyrolysis temperature, which likely increases the need for alkali metal excess, however it is not known whether this need exceeds the 5% used here.

If incomplete pyrolysis is affecting the samples treated at temperatures lower than 550 °C to a significant degree, which has been reported for nanoparticles [54], it also aids in further explaining the uneven, pitting phenomenon affecting the surface of some of the samples, which is thought to be caused by poor wetting of the substrate – especially in those pyrolyzed at 400 °C.

7 Concluding remarks and further work

It is uncertain whether the hypothesis – that the sodium rich epitaxial layer observed in the STO-based samples was cause for the formation of the $(K_{1-x}Na_x)_2Nb_4O_{11}$ phase near the surface – accurately describes the growth environment of 400 °C samples. A clear sodium-gradient has not been successfully observed through the analysis conducted, hence the stipulation it is based on may, in fact not describe the actual situation, and to claim otherwise would be a post hoc fallacy.

Nevertheless, the synthesis method originally developed by K. N. Pham [3] was successfully replicated, and further improvements were made. Additionally, it was found that the improved method is suitable for use with both STO and SiPt substrates, yielding comparable results, slightly favouring STO substrates – which can be attributed to the more suitable lattice match with KNN.

Significant progress towards phase purity has been achieved by increasing the pyrolysis temperature to 550 °C and the implementation of a preliminary cleaning step by means of O_2 plasma in favour of the addition of PVA in the solution, thereby modifying the synthesis route developed by K. N. Pham. No significant cracking has been observed at the current film thickness, hence it is expected that films with increased thickness can be successfully synthesized according to the currently preferred parameters – hot plate at 150 °C and pyrolysis at 550 °C.

Further work should involve piezoelectric measurements to determine how the new growth conditions have affected the samples. For further improvements to phase relations, work should follow in the steps of the route set out by the progress made through an increase of the pyrolysis temperature. Phase purity has not yet been fully achieved, and it is not certain if limiting the approach to merely adjusting the pyrolysis temperature will result in success. Under the new growth conditions, the other synthesis routes deserve a theoretical and potentially experimental re-visit as they could still prove to be the missing piece. Additionally, a further increase in pyrolysis temperature to 600 °C should be considered [54, 55], to allow completion of the epitaxial growth seen in the cross section of the SiPt-500 sample as well as ensuring crystallization of the KNN phase for each layer deposited. Due to the recommended increase in pyrolysis temperature, a 2-step heating program could be considered in addition to the initial drying step, to allow for a separation of precursor burnout and KNN crystallization.

8 References

References

[1] H. Needleman. Lead poisoning. *Annual Review of Medicine*, 55:209–222, 2004.

[2] European Union. Commission delegated directive 2012/50/eu, 2012. UR-Lex - 32012L0050 - EN.

[3] K. N. Pham. *Potassium Sodium Niobate Thin Films by Chemical Solution Deposition*. PhD thesis, NTNU, 2014.

[4] K. K. T. Lorentzen. *Unpublished work, $K_{0.5}Na_{0.5}NbO_3$ deposition on platinized silicon substrates*. Project work, NTNU, 2015.

[5] G. H. Haertling. Ferroelectric ceramics: History and technology. *Journal of American Ceramic Society*, 82(4):797–818, 1999.

[6] S. Katzir. Who knew piezoelectricity? Rutherford and Langevin on submarine detection and the invention of sonar. *The Royal Society Journal of The History of Science*, 2012.

[7] J. Wang. Ferroelectric liquid crystal display and method of manufacturing the same, 2002. US Patent App. 10/020,174.

[8] M. T. Ghoneim, M. A. Zidan, M. Y. Alnassar, A. N. Hanna, J. Kosel, K. N. Salama, and M. M. Hussain. Thin PZT-based ferroelectric capacitors on flexible silicon for nonvolatile memory applications. *Advanced electronic materials*, 1(6):411–418, 2015.

[9] T. Kanda, T. Morita, M. K. Kurosawa, and T. Higuchi. A rod-shaped vibro touch sensor using PZT thin film. *IEEE Transactions on Ultrasonics, Ferroelectrics, and Frequency Control*, 46(4):875–882, 2002.

[10] H. J. Kim, K. Koo, S. Q. Lee, K.-H. Park, and J. Kim. High performance piezoelectric microspeakers and thin speaker array system. *ETRI Journal*, 31(6):680–687, 2009.

[11] Developing new phone camera technology. `http://www.forskningsradet.no/prognett-bia/Nyheter/Developing_new_phone_camera_technology/1253998232281/p1226993636106`.

[12] poLight AS. Tlens — how does it work. `http://polight.com/technology/how-does-it-work/`.

[13] T. R Shrout and S. J. Zhang. Lead-free piezoelectric ceramics: Alternatives for PZT? *Journal of Electroceramics*, Feb. 2007.

[14] M. B. Smith, K. Page, T. Siegrist, P. L. Redmond, E. C. Walter, R. Seshadri, L. E. Brus, and M. L. Steigerwald. Crystal structure and the

paraelectric-to-ferroelectric phase transition of nanoscale $BaTiO_3$. *Journal of American Chemical Society*, 130(22):6955–6963, 2008.

[15] G. H. Haertling. Ferroelectric ceramics: History and technology. *Journal of American Ceramics Society*, 82(4):797–818, 1999.

[16] T. Nagai, K. Iijima, H. J. Hwang, M. Sando, T. Sekino, and K. Niihara. Effect of MgO doping on the phase transformations of $BaTiO_3$. *ETRI Journal*, 83:107–112, 2000.

[17] X. Wang, C.-N. Xu, H. Yamada, K. Nishikubo, and X.-G. Zheng. Electro-mechano-optical conversions in Pr^{3+}-doped $BaTiO_3$-$CaTiO_3$ ceramics. *Advanced Materials*, 17:1254–1258, 2005.

[18] L. Egerton and D. M. Dillon. Piezoelectric and dielectric properties of ceramics in the system potassium-sodium niobate. *Journal of the American Ceramic Society*, 42(9):438–442, 1959.

[19] Y. Saito, H. Takao, T. Tani, T. Nonoyama, K. Takatori, T. Homma, T. Nagaya, and M. Nakamura. Lead-free piezoceramics. *NATURE*, 432, 2004.

[20] X. Chao, J. Wang, X. Xie, P. Liang, and Z. Yang. Tailoring electrical properties and the structure evolution of $(Ba_{0.85}Ca_{0.15})(Ti_{0.90}Zr_{0.10})_{1-x}Li_{4x}O_3$ ceramics with low sintering temperature. *Journal of the American Ceramic Society*, 45(1):802–811, 2016.

[21] X. Wang, J. Wu, D. Xiao, J. Zhu, X. Cheng, T. Zheng, B. Zhang, X. Lou, and X. Wang. Giant piezoelectricity in potassium – sodium niobate lead-free ceramics. *Journal of American Ceramics Society*, 136(7):2905–2910, 2014.

[22] Y. Xu. *Ferroelectric materials and their applications*. North-Holland, 1991.

[23] R. Lopez-Juarez, F. Gonzalez, and M.-E. Villafuerte-Castrejon. *Lead-Free Ferroelectric Ceramics with Perovskite Structure*. InTech Europe, 2011.

[24] R. M. Hazen. Perovskites. *Scientific American*, June(1):52–61, 1988.

[25] D. Damjanovic and R. E. Newnham. Giant piezoelectricity in potassium – sodium niobate lead-free ceramics. *Journal of Intelligent material systems and structures*, 190(3):190–208, 1992.

[26] L. Landau and E. Lifshitz. *Statistical Physics Part I*, volume 5. Butterworth-Heinemann, 1980.

[27] C. Kittel. Theory of antiferroelectric crystals. *Physical review*, 82(5), 1951.

[28] Y. Xu, W. Hong, Y. Feng, and X. Tan. Antiferroelectricity induced by electric field in $NaNbO_3$-based lead-free ceramics. *Applied physics letters*, 104, Feb. 2014.

[29] V. M. Goldschmidt. Die gesetze der krystallochemie. *Die Naturwissenschaften*, 21:477–485, 1926.

[30] K. Singh, S. Acharya, and D. V. Atkare. Qualitative analysis of tolerance factor, electronegativity and chemical bonding of some ferroelectric perovskites through MOT. *Ferroelectrics*, 315:91–110, 2005.

[31] P. Goudochnikov and A. J. Bell. Correlations between transition temperature, tolerance factor and cohesive energy in 2+:4+ perovskites. *Journal of Physics: Condensed matter*, 19(17), 2007.

[32] S. M. Selbach. *Structure, stability and phase transitions in multiferroic $BiFeO_3$*. PhD thesis, NTNU, 2009.

[33] M. Adachi, Y. Akishige, T. Asahi, K. Deguchi, K. Gesi, K. Hasebe, T. Hikita, T. Ikeda, and Y. Iwata. Ferroelectrics and related substances: Oxides part 1: Perovskite-type oxides and $LiNbO_3$ family. *Landolt-Bornstein: Numerical Data and Functional Relationships in Science and Technology - New Series, Group III*, 2001.

[34] J. Ravez, M. Pouchard, and P. Hagenmuller. Chemical bonding, a relevant tool for designing new perovskite-type ferroelectric materials. *Ferroelectrics*, 197(1):161–173, 1997.

[35] M. Kosec, B. Malic, A. Bencan, and T. Rojac. *Piezoelectric and Acoustic Materials for Transducer Applications*. Springer, Jan. 2008.

[36] P. Zhao, B.-P. Zhang, and J.-F. Li. High piezoelectric d_{33} coefficient in Li-modified lead-free (Na, K)NbO_3 ceramics sintered at optimal temperature. *Applied physics letters*, 90, 2007.

[37] Q. Zhang, B.-P. Zhang, H.-T. Li, and P.-P. Shang. Effects of Sb content on electrical properties of lead-free piezoelectric $[(Na_{0.535}K_{0.480})_{0.942}Li_{0.058}](Nb_{1-x}Sb_x)O_3$ ceramics. *Journal of Alloys and Compounds*, 176, 2010.

[38] K. W. Hang V. J. Tennery. Thermal and x-ray diffraction studies of the $NaNbO_3$-$KNbO_3$ system. *Journal of Applied Physics*, 39(10):4749–4753, 1968.

[39] J. Fang, X. Wang, R. Zuo, Z. Tian, C. Zhong, and L. Li. Narrow sintering temperature window for (K, Na)NbO_3-based lead-free piezoceramics caused by compositional segregation. *Physica status solidi*, 208:791–794, 2011.

[40] R. Lopez-Juarez, F. Gonzalez-Garcia, J. Zarate-Medina, R. Escalona-Gonzlez, S. D. de la Torre, and M.-E. Villafuerte-Castrejon. Piezoelectric properties of Li–Ta co-doped potassium–sodium niobate ceramics prepared by spark plasma and conventional sintering. *Journal of Alloys and Compounds*, Dec. 2010.

[41] G. Aylward and T. Findlay. *SI chemical data*. Wiley, 2007.

[42] Y. Zhen and J.-F. Li. Normal sintering of (K, Na)NbO_3-based ceramics: Influence of sintering temperature on deification, microstructure and electrical properties. *Journal of american ceramic society*, 89(12), 2006.

[43] F. Madaro, R. Sæterli, J. R. Tolchard, M.-A. Einarsrud, R. Holmestad, and T. Grande. Molten salt synthesis of $K_4Nb_6O_{17}$, $K_2Nb_4O_{11}$ and KNb_3O_8 crystals with needle- or plate-like morphology. *CrystEngComm*, 13:1304–1313, 2011.

[44] Y. Kizaki, Y. Noguchi, and M. Miyayama. Defect control for low leakage current in $K_{0.5}Na_{0.5}NbO_3$ single crystals. *Applied Physics Letters*, 89, Oct. 2006.

[45] Y. Nakashima, W. Sakamoto, T. Shimura, and T. Yogo. Chemical processing and characterization of ferroelectric (K, Na)NbO_3 thin films. *Japanese journal of applied physics*, 46:6971–6975, 2007.

[46] Y. Zhen and J.-F. Li. Abnormal grain growth and new core-shell structure in (K, Na)NbO_3-based lead-free piezoelectric ceramics. *Journal of the american ceramic society*, 90(11), 2007.

[47] Z. Zhang, J. Yang, Z. Liu, and Y. Li. Evolution of textured microstructure of Li-doped (K, Na)NbO_3 ceramics prepared by reactive templates grain growth. *Journal of alloys and compounds*, 624, Nov. 2015.

[48] R. Saravanan, D. Rajesh, S. V. Rajasekaran, R. Perumal, M. Chitra, and R. Jayavel. Crystal growth and dielectric properties of $Na_{0.5}K_{0.5}NbO_3$ single crystal grown by flux method using B_2O_3 flux. *International Journal of Applied Physics and Mathematics*, 2(3), May 2012.

[49] K. N. Pham. Unpublished pictures, received through Prof. Mari-Ann Einarsrud, 2014.

[50] F. Lai and J.-F. Li. Sol-gel processing of lead-free (Na, K)NbO_3 ferroelectric films. *Journal of sol-gel science and technology*, 42, 2007.

[51] N. J. Phillips S. J. Milne Y.-L. Tu, M. L. Calzada. Synthesis and electrical characterization of thin films of PT and PZT made from a diol-based sol-gel route. *Journal of American Ceramics Society*, 79(2):411–418, 1996.

[52] Y. Zhen, J.-F. Li, K. Wang, Y. Yan, and L. Yu. Spark plasma sintering of Li/Ta-modified (K, Na)NbO_3 lead-free piezoelectric ceramics: Post-annealing temperature effect on phase structure, electrical properties and grain growth behavior. *Materials science and engineering: B*, 176(14), 2011.

[53] C. A. Randall, N. Kim, J.-P. Kucera, W. Cao, and T. R. Shrout. Intrinsic and extrinsic size effects in fine-grained morphotropic-phase-boundary lead zirconate titanate ceramics. *Journal of american ceramic society*, 81(3):677–688, 1998.

[54] G. H. Khorrami, A. Company, and A. Khorsand Zak. Structural and optical properties of (K, Na)NbO_3 nanoparticles synthesised by a modified sol-gel method using starch media. *Advanced powder technology*, 26:113–118, 2015.

[55] C. Kang, J.-H. Park, D. Shen, H. Ahn, M. Park, and D.-J. Kim. Growth and characterization of $(K_{0.5}Na_{0.5})NbO_3$ thin films by a sol-gel method. *Journal of sol-gel science and technology*, 46:85–90, 2010.

9 Appendix

Crucible	**1**	**2**	**3**
25 °C, empty	9.2722	9.1975	10.3004
25 °C, Kao wool	10.174	10.1206	11.1143
200 °C, Kao wool	10.1604	10.106	11.1034
Volume, sol	0.001	0.001	0.001
25 °C, Kao wool	10.1705	10.1163	11.1138
25 °C, Kao wool, 24h later	10.1708	10.116	11.1139
25 °C, Kao wool, sol	11.2658	11.2133	12.2173
200 °C, Kao wool, Nb_2O_5	10.214	10.1615	11.1585
25 °C, Kao wool, Nb_2O_5	10.2247	10.1708	11.1688
Nb_2O_5	0.0536	0.0555	0.0551
Moles Nb_2O_5 in crucible	0.0002017	0.0002088	0.0002073
NAmOx, [M]	0.4033	0.4176	0.4146

Table 6: Detailed information regarding the NAmOx solution calibration. Unit-less data is the respective weights or volumes, in [g] and [ml].